Revisiting the identification of commercial and historical green earth pigments

Agathe Fanost, Alice Gimat, Laurence de Viguerie, Pauline Martinetto, Anne-Claire Giot, Martin Clémancey, Geneviève Blondin, Fabrice Gaslain, Helen Glanville, Philippe Walter, et al.

Revisiting the identification of commercial and historical green earth pigments

Agathe Fanost[a,b], Alice Gimat[a], Laurence de Viguerie[a], Pauline Martinetto[c], Anne-Claire Giot[a], Martin Clémancey[d], Geneviève Blondin[d], Fabrice Gaslain[e], Helen Glanville[a], Philippe Walter[a], Guillaume Mériguet[b], Anne-Laure Rollet[b], Maguy Jaber[a,*]

[a] Sorbonne Université, CNRS UMR 8220, LAMS, case courrier 225, 4 pl. Jussieu 75252 Paris cedex 05, France

[b] Sorbonne Université, CNRS UMR 8234, PHENIX, case courrier 51, 4 pl. Jussieu 75252 Paris cedex 05, France

[c] Univ. Grenoble Alpes, Inst NEEL, F-38042 Grenoble, France

CNRS, Inst NEEL, F-38042 Grenoble, France

[d] Université Grenoble Alpes, CNRS, CEA, DRF/BIG/LCBM (UMR 5249), pmb, F-38054 Grenoble, France

[e] *MINES ParisTech, PSL - Research University, MAT - Centre des matériaux, CNRS UMR 7633, BP 87, F-91003 Evry, France*

*Corresponding Author:

Maguy Jaber

Tel: +33-(0)1-4427-6289

Email: maguy.jaber@sorbonne-universite.fr

Abstract

Green earth is a common green pigment based on celadonite and glauconite, used since Antiquity by artists. Two geological minerals, eight commercial green earth pigments and a sample taken from a historical location in Monte Baldo were characterized. A set of different techniques including X-Ray diffraction (XRD), scanning electron microscopy coupled to energy dispersive spectroscopy (SEM-EDS) and numerous spectroscopies: spectrophotocolorimetry, near and mid infrared, Raman, Mössbauer were used to identify the structure and composition of the different earths. The results highlight complex composition with the presence of various phases, which can be due to the pigment sampling at a different location in the same deposit. Mobile and non-invasive analyses were carried out in order to suggest a protocol for the identification of green earth in artworks, and more specifically to distinguish celadonite and glauconite. With the available mobile non-invasive techniques, and the above analyses on the raw pigments, the green area in Nicolas Poussin's painting, *Bacchanales d'enfants (*Galleria Nazionale d'Arte Antica (GNAA), Rome) was examined as a case study.

Keywords: Green earth, celadonite, glauconite, XRD, Mossbauer, SEM-EDS.

41 **Graphical Abstract**

42

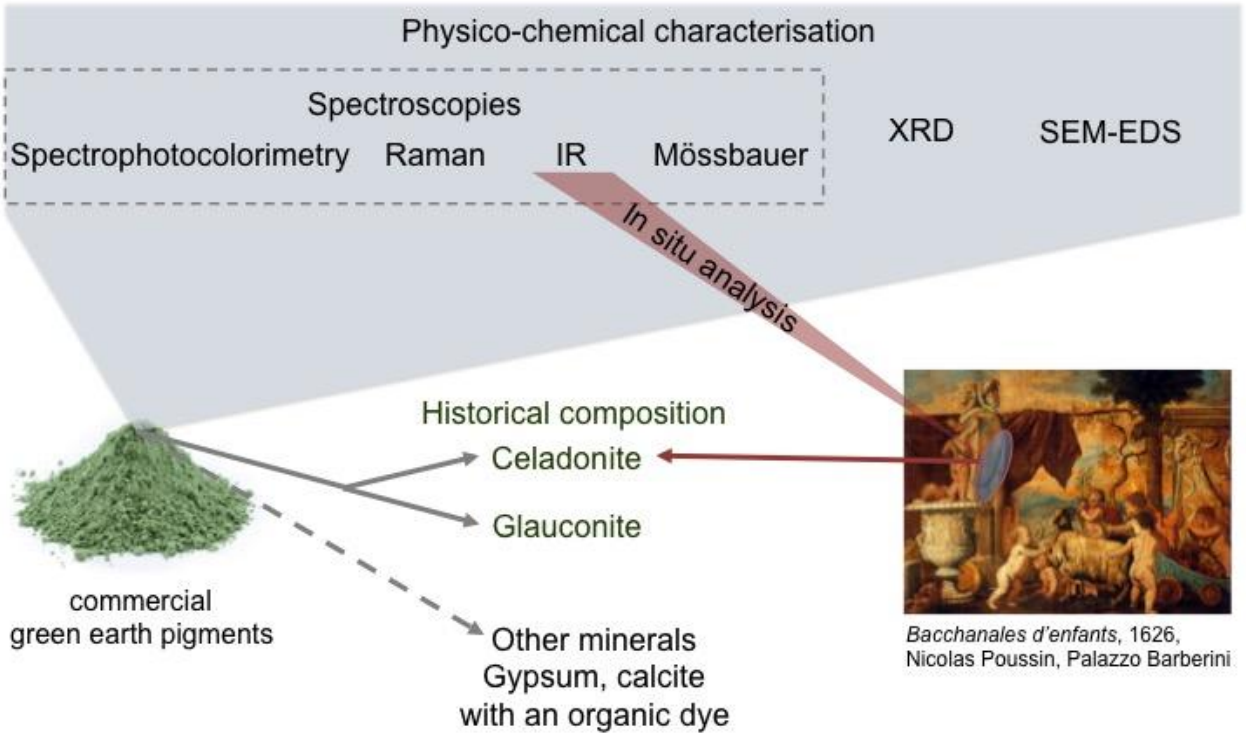

43

44

1 Introduction

Green earth pigments along with malachite ($Cu_2CO_3(OH)_2$) and verdigris (pigment obtained when acetic acid is applied to copper in presence of air), are among the oldest green pigments ever used [1]. During Antiquity, the Romans especially employed them when painting in fresco [2–5] where the pigments are impregnated on a freshly spread moist lime plaster. This technique is well known to fix the colours on the wall. Calcium carbonate migrates through the surface and forms a protective layer by carbonation. Green earth pigments are highly suitable for this technique as they do not react with the lime plaster[6]. From the Middle Ages onwards, they have also been used in tempera paintings. In the latter, the pigments are ground and mixed with a binder that consists in animal glue or egg yolk mixed with water. In Early Italian paintings, the green earth is mostly used as an underlayer for the flesh [7] or as the bole beneath gold-leaf and on occasion for the draperies [8,9]. In later paintings, in Italy, it has also been observed used for greenery in landscapes [10].

Even though the detection of iron has been used to attest the use of green earth pigments in historical artefacts [2,11–14], this should be analysed carefully since iron is present in other pigments such as iron oxides and other earth pigments. While mobile instruments were developed in the last century for the identification of the structure and composition of different pigments, green earths remain difficult to identify[5,15–17]. Green earth pigments are composed of several minerals whose proportions vary depending on the ore deposit. The most abundant ones are celadonite [18,19] and glauconite [20]. Celadonite is formed in vesicular cavities and fractures of volcanic rocks while glauconite is formed in marine sedimentary deposits [20–22]. Consequently,

glauconite is more widely distributed than celadonite. However, the glauconite concentration in the deposit is quite low in comparison to the celadonite one because of their formation processes [20]. Glauconite is more widespread but seems difficult to find; Delamare [5] and Odin [20] reported its occurrence in many locations in France, in Provence or Normandy for instance. Some other authors have identified its presence in Bohemia [15,16,23]. In contrast, celadonite is more easily found. It also can be found in Bohemia [23], in Cyprus and in Monte Baldo near Verona (Italy), this latter deposit is no longer exploited. Furthermore, Cyprus green earth was sold in Smyrna (now Izmir) in Antiquity, leading to a common misinterpretation of its origin [5,21].

The geological literature clearly distinguishes the two minerals from the nature of their deposit. Unfortunately, once extracted and sold as “green earth pigment” their origin becomes difficult to trace, and it becomes even more complicated once the pigment is mixed within the paint with several other compounds.

From a mineralogical point of view, celadonite and glauconite are two phyllosilicates from the mica group [21]. They are composed of an aluminium oxide octahedral layer sandwiched between two silicon oxide tetrahedral layers. However, depending on the formation conditions and on the environment of the deposit, substitutions in tetrahedral or octahedral sheets can occur. Aluminium in an octahedral sheet can be replaced by Fe^{III}, Fe^{II} or Mg^{II}, while silicon is only replaced by aluminium. There are differences in these substitutions between the two minerals. The Si substitution rate is higher in glauconite than in celadonite[18]. Moreover, celadonite contains a larger ratio of divalent ions R^{2+} (Mg^{II} and Fe^{II}) than trivalent ions R^{3+} (Al^{III} or Fe^{III}). In addition, the celadonite R^{2+}/R^{3+} ratio is 1:1 while in glauconite, it is about 2:1, and, the Fe^{II}/Fe^{III} ratio varies

between the two minerals. *Ergo*, this chemical composition could be a main criterion in the identification of the minerals.

Therefore, the identification of celadonite and glauconite in a paint mixture indicates the presence of a green earth. For this purpose, several techniques can be used such as X-ray diffraction (XRD), infrared (IR) spectroscopy, and X-Ray fluorescence (XRF).

Nevertheless, despite numerous studies on clayey materials in various fields ranging from physical chemistry to geoscience, mineralogical analyses in the field of cultural heritage are seldom and often limited to the identification only of the generic class of 'green earth' without any specific details on the mineralogical species present in the artwork [16,24]. This information can however provide further knowledge about the work of painters and their choice of pigment used in relation also to the technique used (aqueous such as *a tempera*, or oil). Hence the detailed investigation of the pigment composition is highly valuable for research in the field of cultural heritage.

In this work, a multi-analytical technique approach is applied to two minerals, eight commercial green earth pigments, and a sample taken in an historical deposit in 2014 where celadonite was mined from the Middle Ages to the 20th century, in order to identify their composition. Moreover, these extensive characterisations enable one to provide a protocol for the identification of celadonite and glauconite in artworks with and without sampling.

2 Materials and methods

2.1 Samples

Eleven samples were chosen for this study: two minerals from the geological and mineral gallery of the *Musée National d'Histoire Naturelle* (MNHN, Paris, France), eight commercial green earth pigments and one green earth sample taken in 2014 from a historical celadonite location in Monte Baldo, near Prà della Stua. Samples were used as received. Sample names and suppliers are listed in Table 1.

Table 1: Samples and references analysed

Compound	Sample Name	Supplier	Reference
Monte Baldo celadonite	Cel_Mon	MNHN	
Villers-sur-mer glauconite	Glau_Vil	MNHN	
Bohemian green earth	GE_Boh	Kremer Pigmente	K40810
Cyprus green earth	GE_Cyp	Kremer Pigmente	K17400
Cyprus blue green earth	BGE_Cyp	Kremer Pigmente	K17410
Russian green earth	GE_Rus	Kremer Pigmente	K11110
Veronese green earth	GE_Ver	Kremer Pigmente	K11000
Brentonico green earth	GE_Bren	Laverdure	346378
Nicosie green earth	GE_Nico	Laverdure	346379
Sennelier green earth	GE_Sen	Sennelier	213
Brentonico green earth	GE_Bren_h	Historical site	

2.2 Colorimetric measurements

Colorimetric measurements were carried out with a device from Ocean Optics composed of a halogen light source HL-2000, optic fibres mono coils UV-Vis of 400 µm diameter and a spectrophotometer USB 4000. Measurements were obtained in reflection mode with an angle of 30° between the incident light and the collector. The exposure time was 5 ms and 300 scans were averaged. An observer at 2° and illuminant D65_1 were chosen to obtain *L*, a*, b** coordinates.

2.3 Scanning electron microscopy

Energy Dispersive Spectroscopy (EDS) analyses were carried out in a Zeiss Sigma 300 SEM equipped with a Bruker Quantax 6030 EDS spectrometer at 20 kV for an acquisition of 500 kcounts. Prior to analyses, each powder sample was dispersed on a stub with double-sided carbon tape and was subsequently coated with a carbon layer by evaporation. Semi quantitative results were calculated using a standardless PB-ZAF method.

2.4 X-ray diffraction

X-ray powder diffraction (XRD) measurements were conducted on a Bruker D8 Advanced diffractometer operated at Cu Kα radiation (λ = 0.15404 nm). XRD patterns were measured using the following parameters: tension of acceleration, 40 kV; current, 40 mA; 2θ values ranging from 5° to 70°; step, 0.020° and step time, 0.75 s.

Synchrotron powder diffraction patterns of five selected samples (GE_Boh, GE_Cyp, BGE_Cyp; GE_Bren and GE_Bren_h) were collected at the European Synchrotron Radiation Facility (ESRF, Grenoble) on the beamline ID22 [25] at an energy of 31 keV (0.03999 nm wavelength) using the high-resolution multi-analyzer setup [26]. The five samples are mounted as received inside cylindrical borosilicate capillaries (0.9 mm diameter). DIFFRAC.*EVA's* (Bruker) *search*/*match* module, which carries out searches on the PDF4+ (2018) reference database, has been used for *phase identification*. All analyses of the X-ray powder diffraction patterns were carried out with the FP_Suite software [27]. First, Le Bail refinements were conducted in order to confirm the phase identification. Rietveld refinements were then carried out to obtain the mass proportion

of the different crystalline phases in the mixtures. The *Inorganic Crystal Structure Database* [28] was consulted to obtain the crystal structures of the phases identified.

2.5 Mid- and Near-Infrared spectroscopy

Mid-infrared spectroscopy was carried out in attenuated total reflectance mode (ATR) on an Agilent Technologies Cary 630 FTIR device equipped with a diamond crystal. Powders were analysed between 650 and 4000 cm^{-1}, with 4 cm^{-1} of resolution and 64 scans.

Near-infrared spectroscopy was conducted with one hyperspectral camera (NIR-SWIR) from Specim (Oulu, Finland). Samples were compressed in pellets. The camera was mounted on a rotation stage to acquire the images in push broom technique, i.e. by scanning the painting horizontally and acquiring full spectral information for one vertical line on the pellets/paintings at a time. The spectral range is 1000 to 2500 nm with 280 wavelength channels and a spectral sampling of 12 nm. During the investigation, diffuse illumination was provided by one 20 W halogen lamp, placed at a distance of 0.4 m. For the pigment pellets, the OLES56 (Specim, focal length 56 mm) was used with a lateral resolution of ca. 130 µm. In this zoom configuration (distance camera-painting of 40 cm), the acquisition parameters were 20 ms integration time, 4 fps and 0.07°.s^{-1} rotation speed. For the painting by Nicolas Poussin: a first objective (OLES30, Specim, focal length 30 mm) was used to image the entire painting with a lateral resolution of approx. 1.5 mm; three scans were acquired with 50 ms integration time, 6 fps (frames per second) and 0.01°.s^{-1} rotation speed. The OLES56 (Specim, focal length 56 mm) was also used on the selected area with a lateral resolution of ca. 130 µm. In this “zoom”

configuration (distance camera-painting of 40 cm), the acquisition parameters were 200 ms for the integration time, 4 fps and 0.07°.s^{-1} for the rotation speed.

The data was normalized with dark and bright field images using the Specim plug-in in ENVI (Harris Corporation, Melbourne, Florida, USA). The spectra were averaged on an area of 4x4 pixels.

2.6 Raman spectroscopy

Raman spectroscopy was used as a complementary tool to identify the organic components in three pigments. An Invia Renishaw spectrometer coupled with a Leica microscope equipped with a 50× objective was used to acquire the Raman spectra. Monochromatic excitation was obtained with a green Nd:YAG laser (532 nm) or red diode laser (785 nm) and the corresponding 1800 $l.mm^{-1}$ or 1200 $l.mm^{-1}$ grating were used to disperse the signal onto the CCD detector. Laser power, exposure time, and accumulations were adapted depending on the sample.

2.7 Mössbauer spectroscopy

Mössbauer spectra were recorded at room temperature on a homemade Mössbauer spectrometer operating in a constant acceleration mode in transmission geometry. The isomer shift values were referenced against that of a room temperature metallic iron foil. Analysis of the data was carried out with the software WMOSS Mössbauer Spectral Analysis Software (www.wmoss.org, 2012-2013 Web research, Edina) and with a homemade program [60]. A Lorentzian profile was considered. The recoil-free fraction was assumed to be independent of the iron location and state, and accordingly, relative content of iron atoms corresponds to the relative area of subspectra.

3 Results and discussion

3.1 Colorimetric measurements

Colorimetric measurements were performed by considering the *CIE L*a*b** colour space. *L** is the lightness from black (0) to white (100). *a** varies from green (-) to red (+) whereas *b** varies between blue (-) and yellow (+). Except for GE_Ver and GE_Bren-h samples, all other green earths presented values of a* varying between -15 and -5, *b** between 0 and 18 and *L** values is in the range 45-70 (Figure 1) matching, indeed, with the green part of the chromatic disc. GE_Bren_h and GE_Ver have a beige colour.

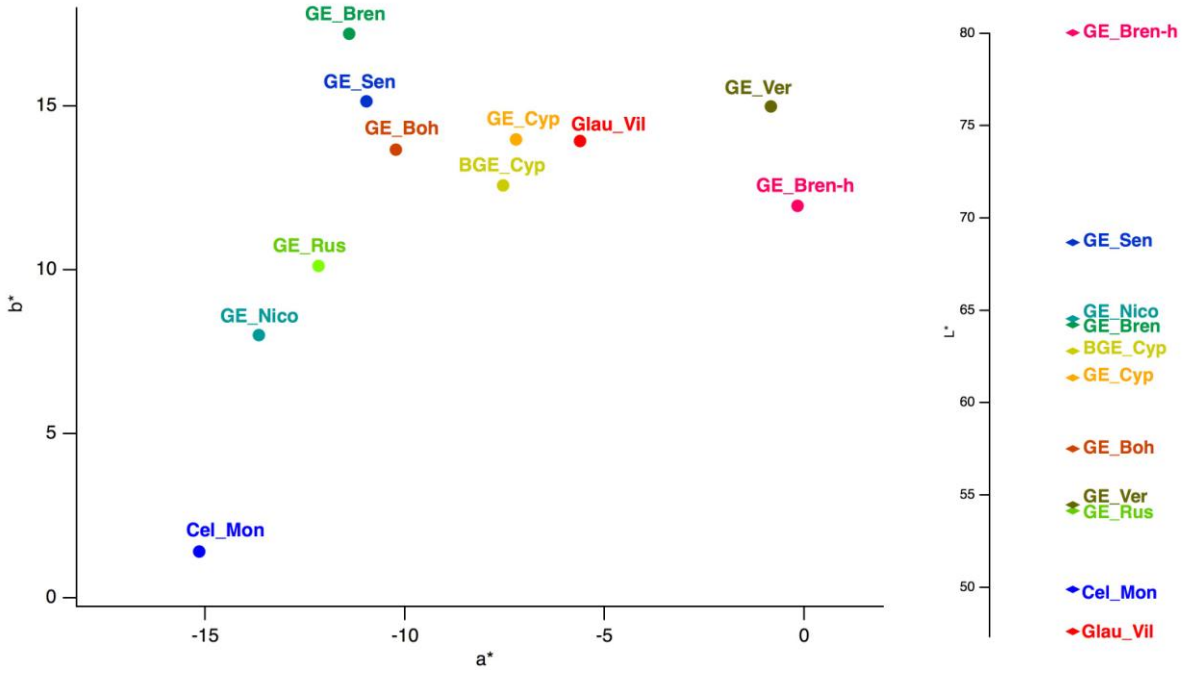

Figure 1: Green earth colour identification in the L*a*b* space

Figure 2 depicts on the left, the visible reflectance spectra of the different samples; we also indicate, on the right of the figure, log(1/R) to make the transition bands associated to the d-d ligand-field transitions responsible of the green colour more visible.

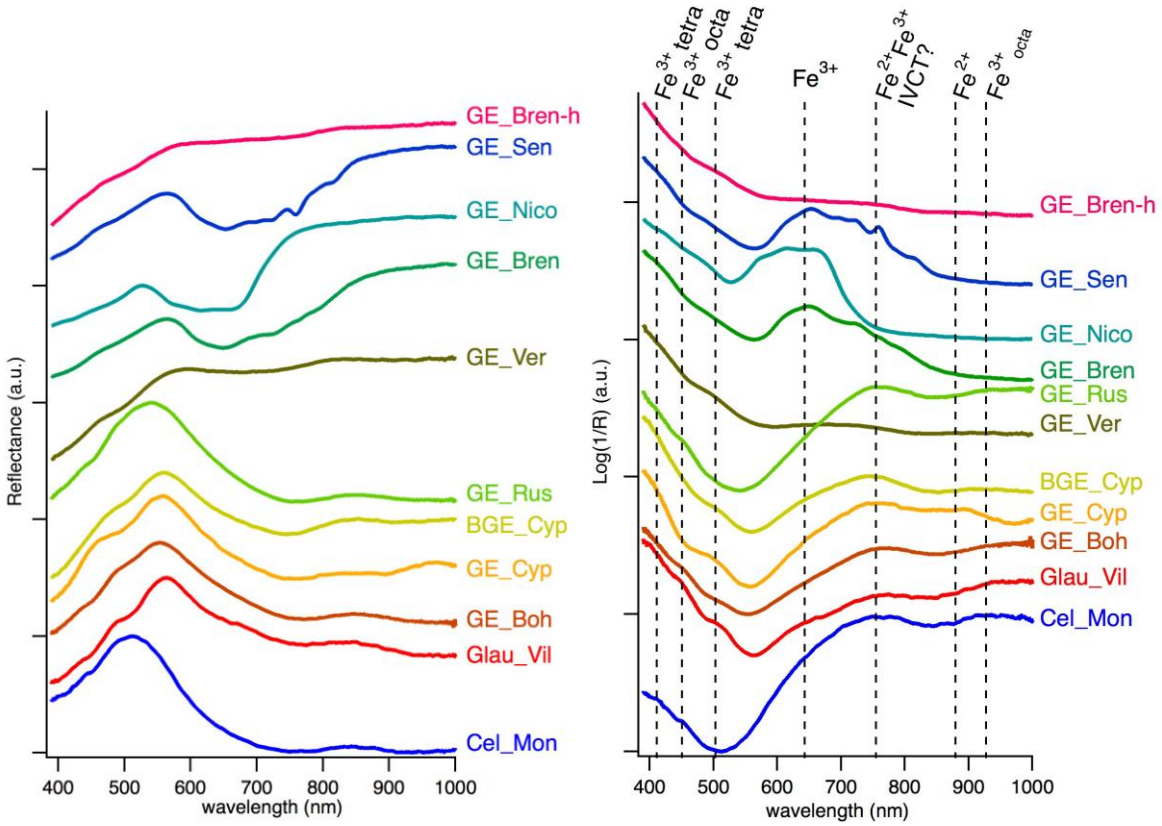

Figure 2: Left: Visible spectra of green earths from 400 to 1000 nm; right: Log(1/R) of the different green earths from 400 to 1000 nm

Assignments are proposed according to Hradil [23]; nevertheless, these transitions are not specific to celadonite nor glauconite, as Hradil also observed.

The commercial pigments can be separated into two different groups:

- GE_Bren, GE_Sen, GE_Nico, GE_Ver, and GE_Bren-h.
- The others, which exhibit characteristic features of celadonite/glauconite.

3.2 Scanning electron microscopy (SEM)

SEM micrographs are illustrated in Figure 3. As for natural minerals, different morphologies have been observed by SEM.

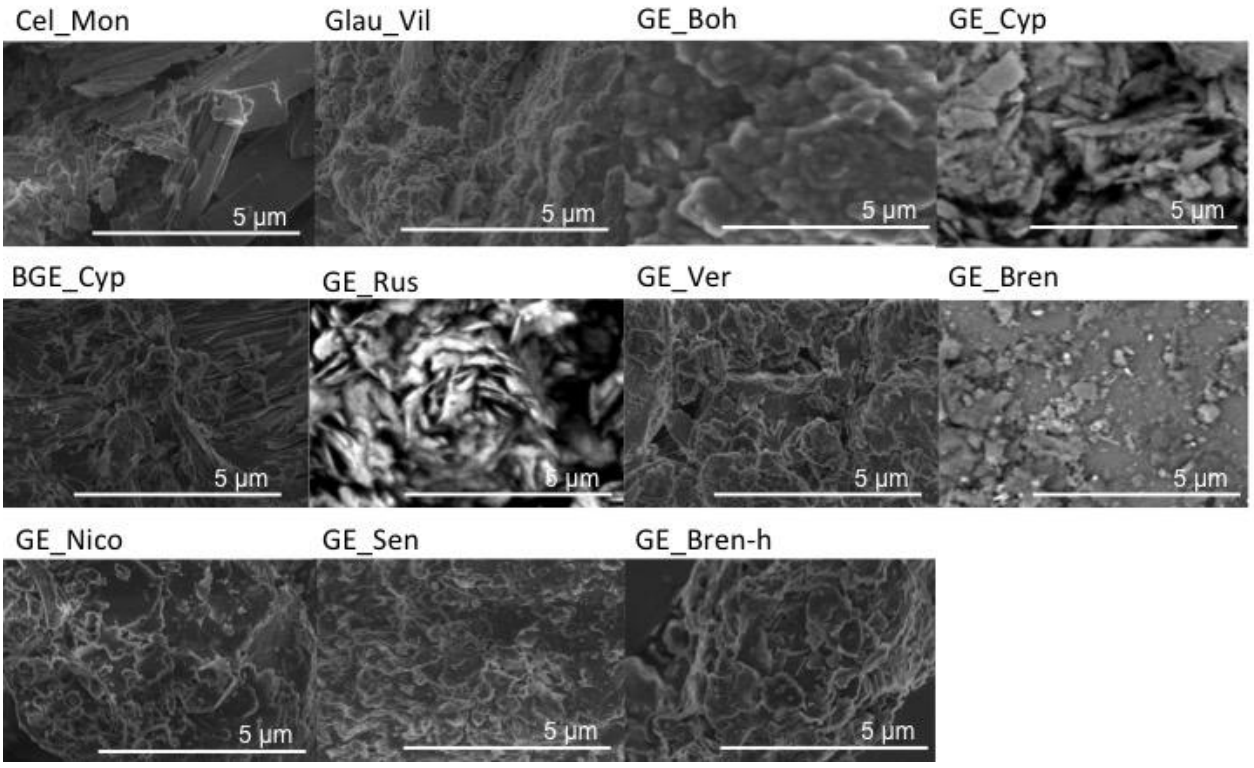

Figure 3: SEM photos of green earths

Cel_Mon and Glau_Vil have the morphology corresponding to celadonite and glauconite respectively, as the literature describes them. Celadonite is composed of rectangular crystals in batten form, which match GE_Cyp according to H. Bearat [29], Moretto [17] and Buckley [18]. Glauconite is less crystalized with a rosette-shape [17,29], it could be attributed to GE_Rus and GE_Boh. On the contrary, GE-Bren, GE_Nico and GE_Sen particles appear flatter and bigger. Their layers seem well compacted compared to the other green earths, and do not look like phyllosilicates.

3.3 XRD measurements

Figure 4 shows the XRD patterns collected with a laboratory diffractometer for the whole set of the samples.

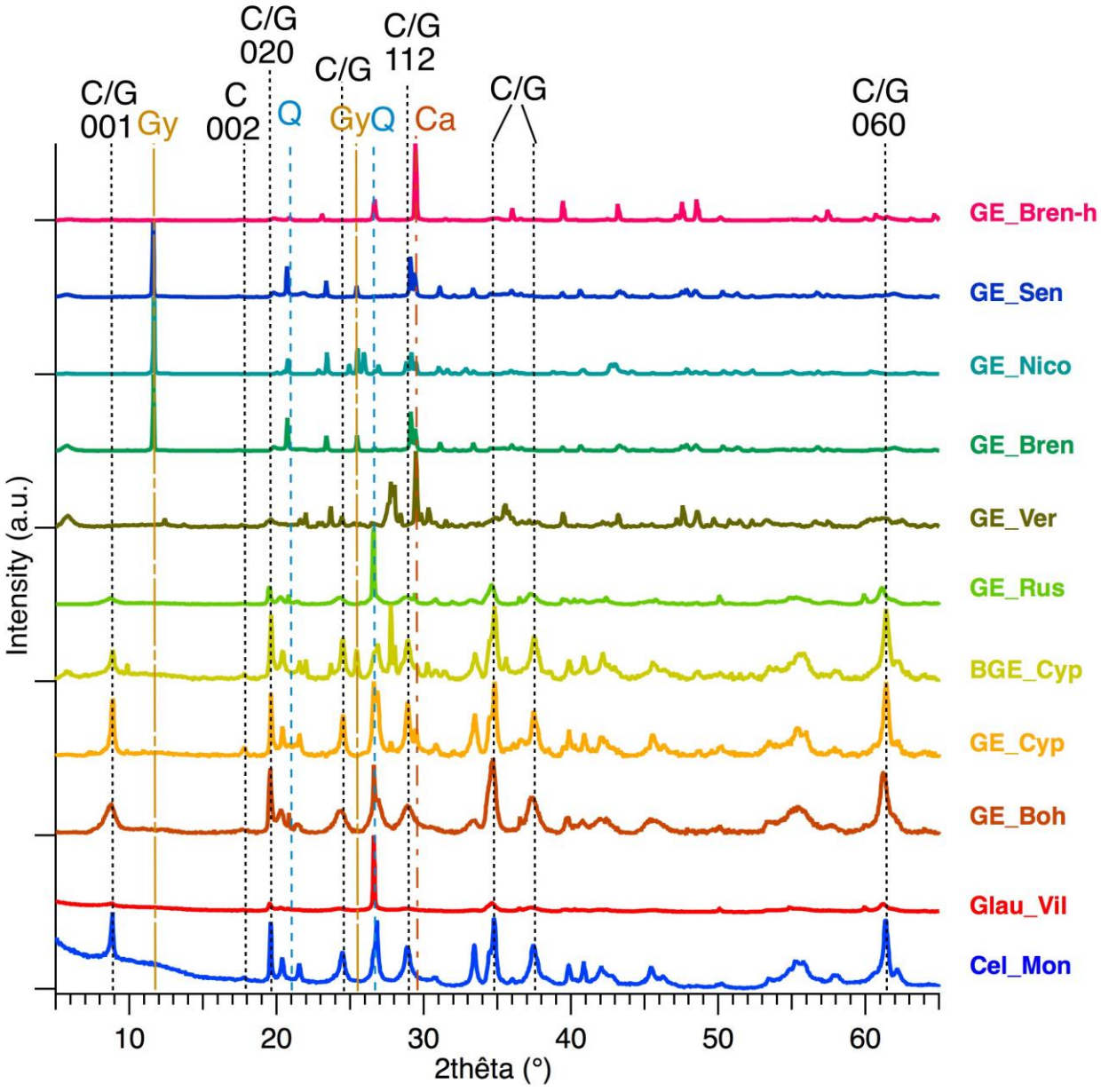

Figure 4: XRD laboratory patterns of two references from mineralogy gallery (Cel_Mon and Glau_Vil), eight commercial green earths and one sample form Brentonico. Most

intense diffraction peaks are attributed with: C: Celadonite, G: Glauconite, Gy: Gypsum, Q: Quartz and Ca: Calcite

Even though existing databases (EVA, Bruker) in XRD allow the identification of crystalline phases (Table 2), and that some studies [30] identify celadonite from a partial pattern, which is debatable, it seems more complicated since the targeted phases are very close from a crystallographic point of view. Moreover, the presence of a mixture of phases in natural samples makes the assignment even more difficult.

Table 2: Mineralogical compositions of the green earths obtained from XRD data (in bold, synchrotron data were used to identify the phases of these samples. In italic, minor phases)

Sample	Main composition identified by XRD (PDF N°)
Cel_Mon	Celadonite (04-014-0727)
Glau_Vil	Glauconite (00-063-0583) Quartz (00-046-1045)
GE_Boh	Mixed-layer celadonite (49-1840) Quartz (86-1560) Montmorillonite (13-0135) *Dickite (10-0446)* *Azurite (01-0564)*
GE_Cyp	Celadonite (49-1840) Quartz (86-1560) Calcite (05-0586) Montmorillonite (13-0135) *Anorthite (18-1202)* *Heulandite (76-0532)*
BGE_Cyp	Celadonite (49-1840) Anhydrite (37-1496) Montmorillonite (13-0135) Anorthite (18-1202) *Heulandite (76-0532)*
GE_Rus	Glauconite (00-009-0439) Quartz (00-046-1045) Calcite (01-066-0867)
GE_Ver	Calcite (01-066-0867) Anorthite (00-018-1202)

GE_Bren	Gypsum (05-0586) Calcite (05-0586) Montmorillonite (13-0135) Quartz (86-1560) *Muscovite (76-0668)* *Anhydrite (37-1496)*
GE_Nico	Gypsum (00-021-0816) Calcite (01-066-0867) Quartz (00-046-1045) Montmorillonite ? (00-029-1499)
GE_Sen	Gypsum (00-021-0816) Calcite (01-066-0867) Quartz (00-046-1045) Montmorillonite ? (00-029-1499) Vanadium borate ? (04-015-9917)
GE_Bren-h	Calcite (05-0586) Quartz (86-1560) Montmorillonite (13-0135) Muscovite (76-0668) *Orthoclase (75-1190)*

According to the literature, the value of the d_{060} is crucial for the distinction between celadonite or glauconite. Indeed, for $d_{060} < 0.151$ nm, dioctahedral celadonite is present and for $d_{060} > 0.151$ nm, trioctahedral glauconite is identified [19,20]. Based on this parameter, Ge_Cyp and BGE_Cyp earths are attributed to celadonite [15,16]. GE_Boh and GE_Rus match with glauconite.

The XRD patterns of GE_Ver, GE_Nico, GE_Bren, GE_Sen and GE_Bren-h do not show any reflexion of celadonite or glauconite, but more those of montmorillonite, gypsum, calcite and/or quartz. GE_Bren_h is mainly composed of smectites.

Because the GE_Boh powder presents broader diffraction peaks than the GE_Cyp and BGE_Cyp powders, indicating an ill-ordered structure, the identification of the clayey mica is more challenging. Particular attention has already been paid to the green earth mined in the Bohemia deposit [16,18,23]. These earlier studies showed that the samples

from Bohemia have characteristics, which differ from pure celadonites or pure glauconites and have to be described as mixed-layer celadonites. Here, the position of the d_{060} diffraction line, equal to 0.1512 nm, is close to that published by Hradil et al. [16], for an interlayered celadonite/smectite sample: 0.1511 nm.

In order to confirm phase identification, synchrotron powder diffraction was used (see Experimental); the whole pattern fitting of synchrotron data has been performed on the basis of the crystallographic data (lattice and structural parameters) found in the PDF4+ and ICSD databases for the respective crystalline phases. In a first step, the diffraction patterns were analyzed by Le Bail refinements (which does not require any structural information except approximate unit cell parameters). For the GE_Boh, the lattice parameters of celadonite were used because no mineral is referenced as “mixed-layer celadonite” or “interlayered celadonite/smectite” in the PDF4+ database. The background was estimated by linear interpolation between selected points between Bragg peaks. An isotropic pseudo-Voigt function was used to describe the peak shapes, except for celadonite, which shows a strong anisotropic broadening. In this latter case, the Thompson-Cox-Hastings function with spherical harmonics expansion was implemented to account for the anisotropic peak broadening. Globally, the reliability factors reached for the main phases were satisfactory and the main residuals on the difference line resulted mainly from profile errors and from the presence of some minor peaks, which are still unidentified (Figure 5). In a second step, we conducted Rietveld refinements: an overall isotropic atomic displacement parameter, common to all atoms of a given phase, was refined and the atomic positions and occupancy parameters were kept fixed at the values found in the references. In the ICSD database, three entries can be found for celadonite and we chose this corresponding to a Fe-rich celadonite with the

composition $K(Fe_{1.51}Mg_{0.41}Al_{0.05})((Si_{3.94}Al_{0.06})O_{10})(OH)_2$. In the final Rietveld refinement, profile parameters and structural parameters have been simultaneously refined. Powder diffraction pattern of the GE_Boh mineral was not treated by the Rietveld method because we have given up on determining the crystal structure of the mixed-layer celadonite because of the presence of other crystalline phases in the powder. Moreover, minor phases (estimated to less than 1% in mass) were not taken into account in the Rietveld refinements. Quantitative phase analysis was derived from the scale factors to assess the pigments composition. The mass proportions are summarized in Table 3 and Figure 6 shows the Rietveld refinement results for samples GE_Cyp and GE_Bren.

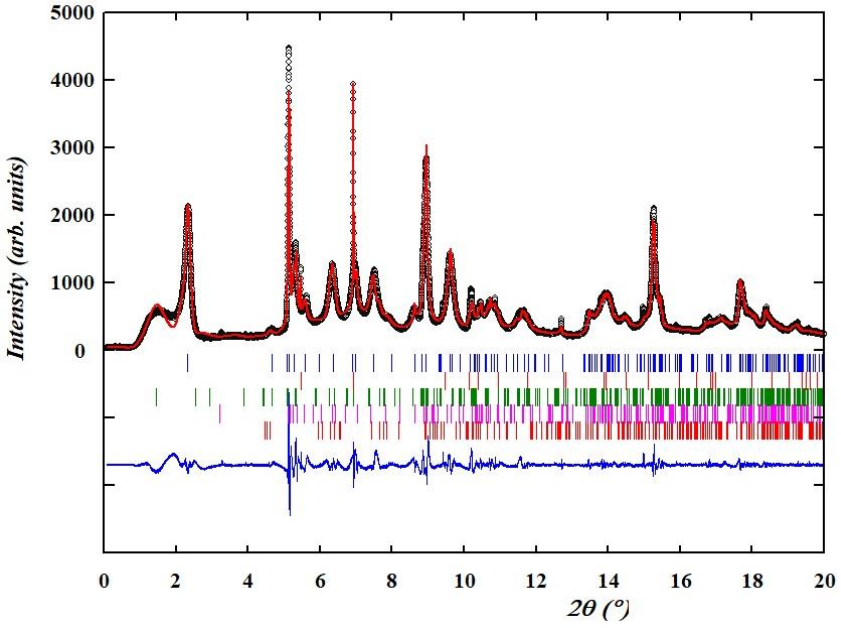

a.

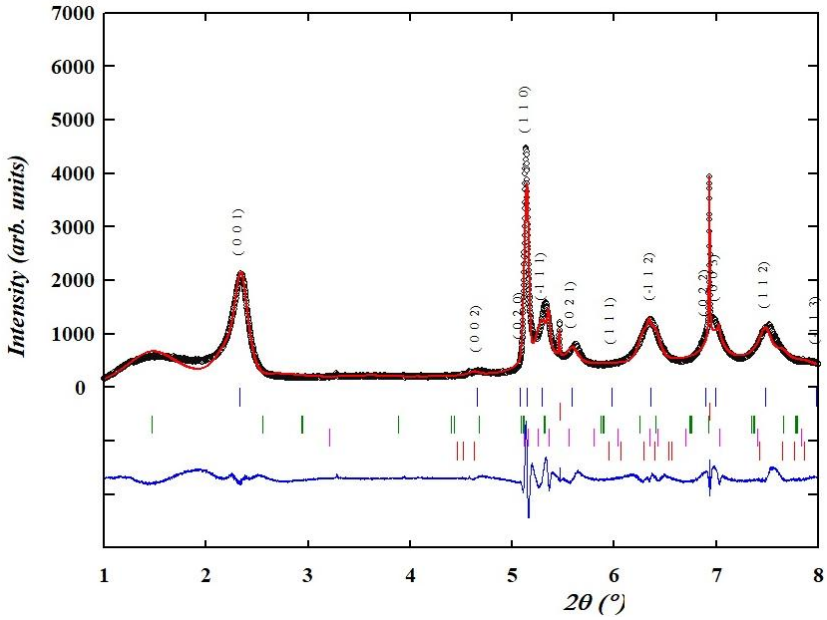

b.

Figure 5: **a. (top)** Le Bail refinement result for sample GE_Boh (experimental pattern: data points, calculated pattern: red full line, difference: blue full line. The vertical ticks indicate the Bragg positions for celadonite, quartz, montmorillonite, dickite and azurite respectively), Rwp = 18 % (chi2=9.8). The unit-cell parameters obtained for celadonite are: a = 5.2182(11) Å, b = 9.0312(17) Å, c = 10.0180(43) Å, β = 100.76(4)°. **b. (bottom)** Strong hkl-dependent anisotropy of the diffraction profiles of celadonite: see for example broadening of (001) and (110) Bragg reflections.

In the green earths analysed at ESRF, compositions are shown in the Table 3.

Table 3: Phase quantification by Rietveld refinements (%wt) Standard deviations of the refined parameters were scaled with the Berar factor [31].

Samples	Celadonite	Montmorillonite	Muscovite	Quartz	Calcite	Gypsum	Anhydrite	Anorthite

GE_Cyp	**70(3)**	16(2)		8(1)	6(1)			
TBV_Cyp	**66(3)**	18(1)					5.0(1)	11(1)
GE_Bren		33(1)		1.0(3)	21(1)	**45(2)**		
GE_Bren_h		11.2(8)	5.8(6)	18(1)	**65(2)**			

302

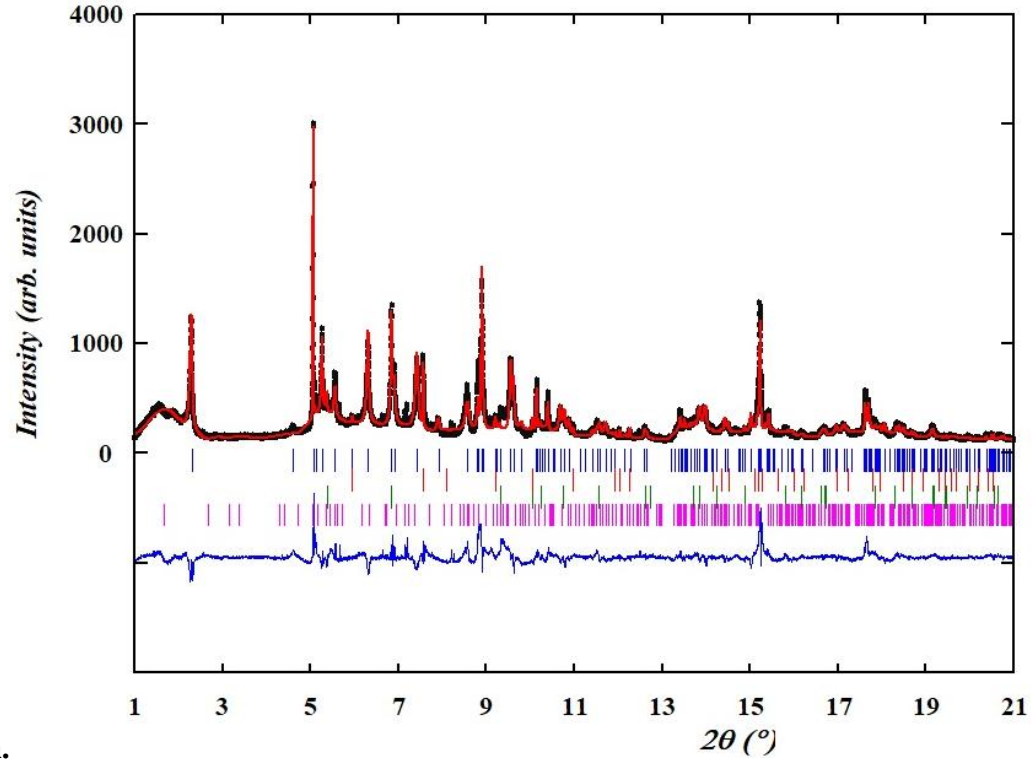

303 **a.**

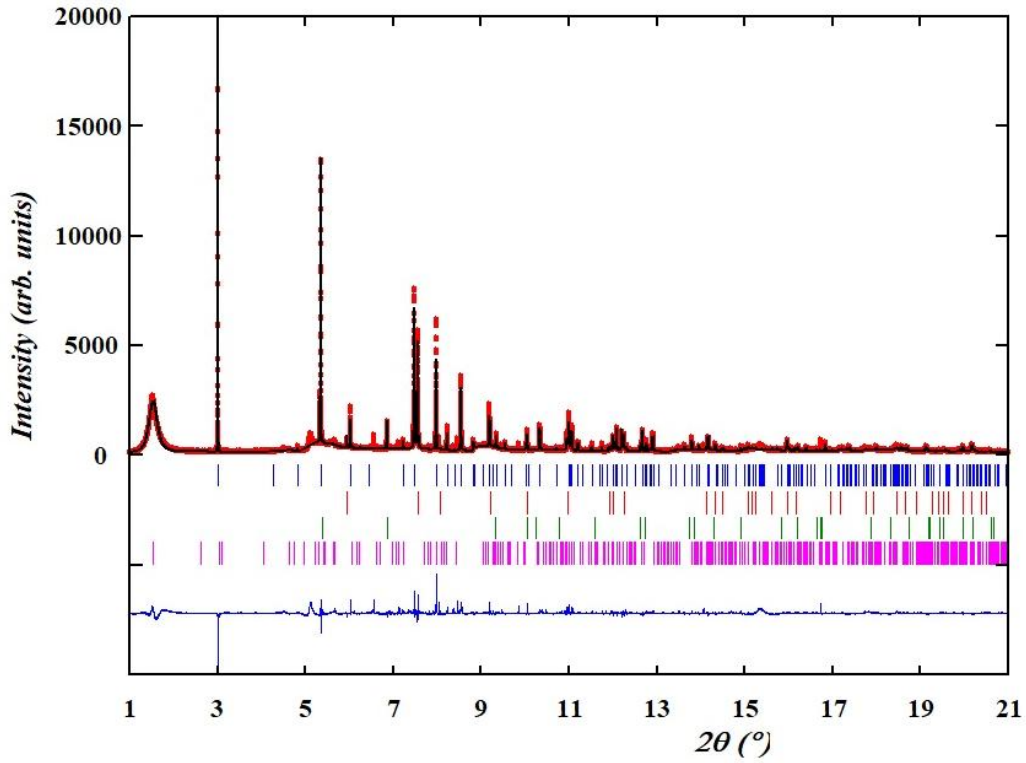

b.

Figure 6: Rietveld refinement results (experimental pattern: data points, calculated pattern: red full line, difference: blue full line) for samples GE-Cyp (a, top), Rwp = 32 % (Chi2=16.2). The vertical ticks indicate the Bragg positions for celadonite, calcite, quartz and montmorillonite respectively and GE_Bren (b, bottom), Rwp = 25 % (chi2=15.2). Bragg positions for gypsum, calcite, celadonite, quartz and montmorillonite, respectively.

3.4 SEM-EDS

EDS results are presented in **Erreur ! Source du renvoi introuvable.**. Celadonite and glauconite can be distinguished thanks to their chemical composition.

Table 4: EDS results

Samples	%mol														
	Si	Mg	Al	K	Fe	Na	Ca	P	S	Ti	Cl	Cu	Sr	Ba	Co
Cel_Mon	20.94	3.81	0.63	5.75	7.82										
Glau_Vil	16.2	2.01	4.03	3.16	5.36		0.37		0.08						
GE_Boh	20.80	2.21	5.06	4.03	5.87	0.54	0.08	0.08	0.14						
GE_Cyp	16.74	4.35	2.30	2.33	5.97	0.79	1.68	0.24	0.19	0.24	0.05				
BGE_Cyp	19.22	2.72	2.97	2.57	4.23	0.58	0.78		0.29	0.26					
GE_Rus	20.46	1.46	3.64	3.20	8.30	0.19	1.48	0.68	2.20	4.25					
GE_Ver	16.91	4.31	4.40	0.70	3.49	0.96	5.55	0.06		0.18					
GE_Bren	6.73	0.58	3.14	0.51	8.27	0.36	7.76	0.12	10.24	0.64	2.74	0.50	12.16	14.81	
GE_Nico	0.00	0.00	0.00				11.17		8.09					8.85	0.49
GE_Sen	8.09	0.45	2.82	0.16	0.90	0.08	8.07	0.02	3.62	0.14	0.07				
GE_Bren-h	17.94	0.95	3.86	0.86	0.88	0.21	5.72	0.17		0.03					

Different criteria have been reported in the literature and are listed in the Table 4.

Table 4: Identification of celadonite, glauconite and ferroceladonite in the literature

References	Celadonite	Glauconite	Ferroceladonite
Ospitali, 2008 [15]	Si > Mg > Al	Si > Al> Mg	Si > Mg ~ Al
Moretto, 2011 [17]	Si/Al ≥ 10 Si/Mg < 10 Si/K ≤ 5 Mg/Al > 1	Si/Al < 10 Si/Mg ≥ 10 Si/K > 5 Mg/Al < 1	
Hradil, 2011 [16]	1 < K/(Si/Al) < 1.5	K/(Si/Al) ~ 2	

The references Cel_Mon and Glau_Vil confirm the attribution parameters of Ospitali and Moretto but that of Hradil does not seem applicable to the samples, their values are too high in comparison to the described ones. They are attributed to celadonite and glauconite respectively.

GE_Cyp is therefore attributed to celadonite with Ospitali criteria. GE_Boh, GE_Rus are mainly composed of glauconite. The presence of smectite minerals, such as

montmorillonite, does not significantly affect the ratio reported above since the decrease in potassium content is offset by the increase in aluminium.

With regard to BGE_Cyp and GE_Ver, they could be identified as ferroceladonite as they have the same quantity of Mg and Al, however, GE_Ver might only contain smectite, as the presence of iron that could be iron (III) oxide, also matches with its brownish colour. GE_Bren-h, which is quite similar in aspect to GE_Ver, might also contain a smectite as it contains a small amount of iron, which could be similar to GE_Ver.

Moreover, GE_Bren, GE_Nico and GE_Sen also have a weak presence of phyllosilicate atoms in comparison to sulphur and calcium, which correspond to calcite and gypsum. A low content in Ba is consistent with barite for GE_Bren and GE_Nico. The unusual occurrence of chlorine in two samples, GE_Bren and GE_Sen, could be due to the addition of green dyes such as chlorinated Cu phtalocyanine “phtalo green”, or triarylmethane dye “malachite green”, as has already been reported in the literature on others pigments [15], although no mention could be found in the suppliers’ data sheets. The composition of GE_Nico contains Co indicating the probable presence of cobalt blue.

3.5 Near infrared and infrared spectroscopy

Figure 7 depicted the FT-IR spectra of the different samples.

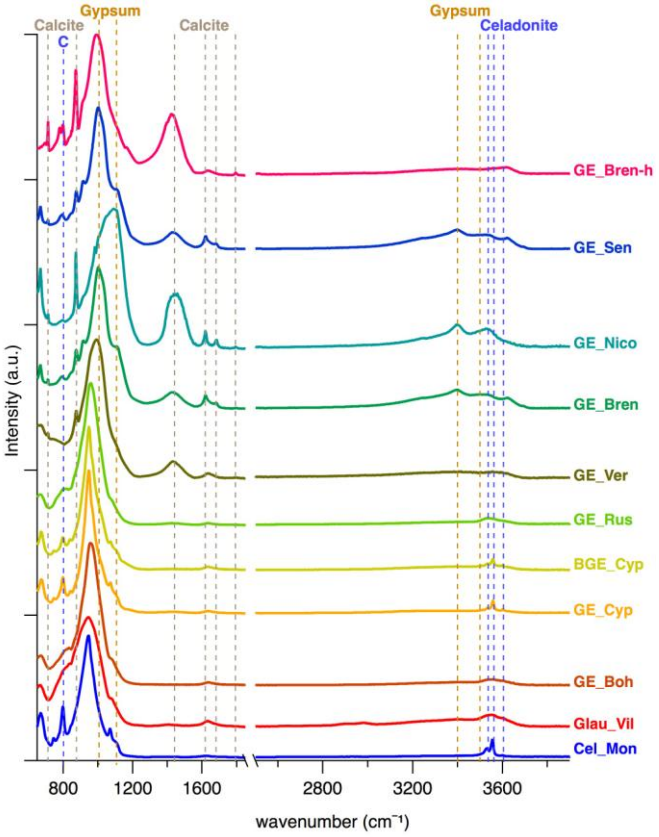

Figure 7: mid-IR reflectance spectra with the main celadonite, calcium, and gypsum attributions in dotted lines (resp. blue, grey and ochre).

Information related to iron and other metallic cation interactions with oxygen can be drawn from the OH stretching region [32,33] (3000-3600 cm^{-1}) and absorption bands in the 650 and 900 cm^{-1} range, which assignments are detailed in Table 5.

The presence of three bands in the regions 3500-3600 cm^{-1} (3534, 3555 and 3601 cm^{-1}) characteristic of the stretching vibrations of the hydroxyl groups correlated to the cations in the octahedral sheet, and 950-1075 cm^{-1} related to the stretching vibrations [15–17] of the tetrahedral sheets is typical of celadonite. A shoulder around 1110 cm^{-1} is observed also for all glauconite samples. This band is assigned to a decrease in the symmetry of the structure of the tetrahedral silicate layers due to the substitution of silicon ions by aluminium ions [34,35]. Other bands at 842, 798, 746 and 673 cm^{-1} are attributed to the

OH bending modes bound to octahedral cations in celadonite [15–17,36]. GE_Cyp and BGE_Cyp, are therefore attributed to celadonite while GE_Rus, GE_Boh to glauconite. GE_Ver, GE_Sen, GE_Nico, GE_Bren and GE_Bren-h contain more gypsum, calcite and smectite. Details on the different bands and their attributions are depicted in Table 5.

In GE_Bren, GE_Nico and GE_Senn, bands at 874 and 712 cm^{-1} are a signature of calcite [37].

Gypsum yields to a wide band between 1100 and 1200 cm^{-1} due to the presence of sulphate ions [37], and calcite at 1430 cm^{-1} due to that of carbonate ions.

Regarding more specifically GE_Bren, GE_Sen and GE_Nico commercial green earths, (Figure 7), the presence of bands at 1793 and 1618 cm^{-1} could also be respectively associated with the presence of cyclic anhydride (1800-1760) and the scissoring in plane of primary amine (N-H) (1650-1590) [38]. Moreover, for these green earths, bands within the 650-900 cm^{-1} range could correspond to C=C stretching of aromatic rings in line with Csp^2-H out of plane bending bands. They are located around 801 cm^{-1} and 671 cm^{-1}, which suggest rather a metal coordination with the aromatic ring. These bands could be the signature of green pigmosol pigment.

379

Table 5: Main bands (cm^{-1}) in green earths mid-infrared spectra and attributions

Samples											Attribution
Cel_Mon	Glau_Vil	GE_Boh	GE_Cyp	BGE_Cyp	GE_Rus	GE_Ver	GE_Bren	GE_Nico	GE_Sen	GE_Bren-h	
669.06	669.06	669.1	672.9	672.9	669.1	668.2	668.2	668.2	668.2	668.2	OH bending vibration
										694.3	
						712	712	712	712	712	$CaCO_3$
745.47			746	745							octahedra cation - OH bending vibration
										779	
797.65			799.6	798			793	795	794	797	lattice deformation and SiO bending band
	816.3	819.2			814						FeFeOH bending band
		832.8									bending of OH bounded to octahedric cation
			842	839							OH bending with octahedric cation, AlOMgOH
							848				
						875.1	874.2	872.3	874.2	872.3	$CaCO_3$
		905.9									bending of OH bounded to octahedric cation
							915	920.8	914	914	OH bending with octahedric cation, AlOAlOH
946.74	946.74	959	946.9	947	957.1						SiO_4 stretching in plane
			968.3	969.2							SiO distortion in plane
						989		982.3		989.7	SiOSi(Al)
				1011			1002	1003.7	1001.8		SO_4^{2-} gypsum
1069.7		1076.4	1071	1071.7							SiO distortion in plane
	1079.1				1081.1						SiO stretching; SiO distortion perpendicular to plane influenced by substitution
								1092			
				1108.1			1108		1104		SO_4^{2-} gypsum
										1165	
						1430.5	1430	1430	1430.5	1425	CO_3^{2-} asymetric stretching
							1617.9	1617.9	1617.9		$CaCO_3$ hydration water
		1635.6	1635.6	1636.5	1636.5	1635.6				1635.6	OH torsion; water in silicates
							1681.2	1685	1680.3		CO^{3-} asymetric stretching
							1794	1794	1793.1	1793.1	$CaCO_3$ hydration water
							3395.1	3400	3400		Water in gypsum
							3529.3	3529.3			Water in gypsum
3529.8		3534	3534	3532.1	3538						OH stretching with $Fe^{3+}OFe^{3+}$
3555.9	3555.9	3558.2	3558.2	3557.2		3558.2					OH stretching with $AlOFe^{2+}$, $MgOFe^{3+}$
3600.6	36006.2	3598.3	3602	3602							OH stretching with AlOMg
							3621.6	3631.8	3620	3616	OH stretching with AlOAl

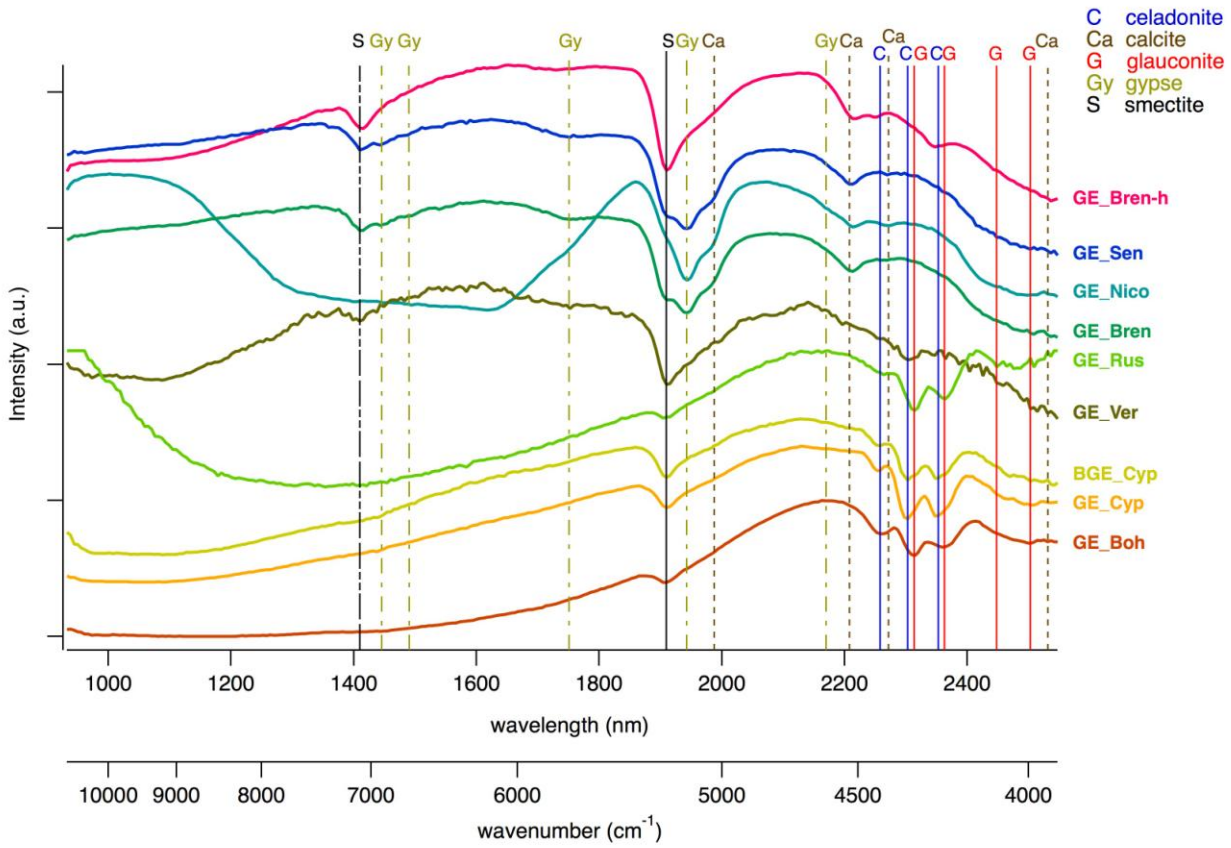

Figure 8: NIR spectra of green earths and main band attributions

With regard to the near infrared region (Figure 8), two sets of pigments could be distinguished. The first set gathered pigments containing celadonite or glauconite which display four bands [36] in the 4000-4500 cm^{-1} range (2200-2500 nm): celadonite has vibrations around 4430 cm^{-1}, 4344 cm^{-1}, 4259 cm^{-1} and 4049 cm^{-1} corresponding for the first three to Al-O-Fe^{3+} or Al-O-Mg, Fe^{3+}-O-Fe^{3+} and Mg-O-Mg-O-Mg hydroxyl combinations, respectively. Those bands were found in GE_Cyp and BGE_Cyp. Bands at 4316 cm^{-1}, 4227 cm^{-1} corresponding respectively to Fe^{3+}-O-Fe^{3+} and Fe^{2+}-O-Fe^{2+}-O-Fe^{2+} hydroxyl combination vibrations [36] attributed to glauconite were identified in GE_Rus and in GE_Boh. The water combination band is identifiable for all samples around 5236 cm^{-1}.

394 The second group (Figure 8) has absorption bands related to either gypsum (GE_Bren,
395 GE_Nico and GE_Sen) or calcite (GE_Ver and GE_Bren-h) depending on their main
396 phases. Gypsum displays intense bands [39] around 4608, 5140, 5730 and 6700 cm^{-1}
397 clearly visible on the spectra of green gypsum-rich pigments (GE_Nico, GE_Bren, and
398 GE_Sen).
399 Unlike gypsum, calcite presence is more difficult to assess by near infrared absorption
400 only due to a superimposition of its sharper band with green earth pigments absorption
401 region.

Table 6: SWIR Near-infrared main band attributions

Samples																		Attribution
GE-Boh		GE_Cyp		BGE_Cyp		GE-Rus		GE-Ver		GE_Bren		GE_Nico		GE_Sen		GE_Bren-h		
nm	cm^{-1}	nm	cm^{-1}	nm	cm^{-1}	nm	cm^{-1}	nm	cm^{-1}	nm	cm^{-1}	nm	cm^{-1}	nm	cm^{-1}	nm	cm^{-1}	
								1410	7092	1410	7092			1410	7092	1.416	7062	Smectite (1920 nm) water harmonique [36]
								1446	6916	1446	6916	1446	6916	1446	6916			Gypsum (1446 nm) combinaisons [39,40]
								1490	6711	1490	6711	1490	6711	1490	6711			Gypsum (1490 nm) combinaisons [39,40]
								1751	5711	1751	5711			1751	5711			Gypsum (1751 nm) hydroxyle/water [39,40]
1910	5236	1910	5236	1910	5236	1910	5236	1910	5236	1910	5236			1910	5236	1910	5236	Smectite (1920 nm) water combinaison [36]
										1943	5147	1943	5147	1943	5147			Gypsum (1944 nm) water [39,40]
										1983	5043	1988	5030	1983	5043			Calcite (1995 nm) v1+3v3 [40–42]
										2170	4608	2170	4608	2170	4608			Gypsum (2170 nm) 3v3 S-O ou OH/H_2O[39,40]
										2208	4529	2208	4529	2208	4529			Calcite (2171 nm) 2v1+2v3 [40–42]
																2219	4507	AlOAl (Montmorillonite) [36]
2258	4429	2253	4439	2258	4429													$AlOFe^{3+}$ (ou Mg) (celadonite) [36]
										2272	4401	2272	4401	2272	4401			Calcite (2265 nm) [40–42]
		2303	4342	2303	4342			2303	4342									$Fe^{3+}OFe^{3+}$ (celadonite) [36]
2314	4322					2314	4322											$Fe^{3+}OFe^{3+}$ (glauconite) [36]
		2348	4259	2353	4250											2348	4259	MgOMgOMg (celadonite) [36]
2364	4230					2364	4230											$Fe^{2+}OFe^{2+}OFe^{2+}$ (glauconite) [36]
						2448	4085	2448	4085									additional band (glauconite) [36]
		2470	4049	2470	4049													additional band (celadonite) [36]
						2476	4039											additional band (glauconite) [36]

2503	3995																	additional band (glauconite) [36]
		2532	3949	2532	3949					2532	3949	2532	3949	2532	3949			Calcite (2532 nm) v1+2v3 [40–42]

403

404

405

3.6 Raman

Raman spectroscopy was also carried out as a complementary tool to identify the presence of organic additives (table S1).

In two commercial green earths GE_Sen and GE_Bren, the signatures of an organic pigment were observed. They were attributed to pigmosol green, a copper chlorinated phtalocyanine, since they matched the reported values of Duran [43].

In GE_Nico were found bands associated with cobalt blue Co-O vibrations, which is in agreement with the presence of cobalt in EDS analysis. In this sample, the presence of barite and hematite was also identified.

3.7 Mössbauer spectroscopy

Mössbauer spectroscopy is an appropriate tool to investigate iron compounds and has been used to investigate soil materials and minerals [44,45]. Five samples were investigated, the two minerals from the MNHN, two commercial green earth pigments, namely GE_Boh and GE Cyp and the sample from the historical location GE_Bren-h. Only GE_Cyp shows large background absorption suggesting the presence of a magnetic iron species such as iron oxide/hydroxide (Figure S1). This contribution amounts to 27±5 % of the total iron content and was subtracted.

Table 7: Mössbauer spectral parameters of investigated samples. Uncertainties are indicated in parentheses

Sample	Doublet	δ (mm.s^{-1})	ΔE_Q (mm.s^{-1})	Γ (mm.s^{-1})	%	%$_{Total}$
GE_Boh	A	0.34(1)	0.40(2)	0.46(2)	68(1)	87(3)
	B	0.33(4)	0.99(6)	0.44(6)	19(2)	
	C	1.24(4)	2.55(8)	0.23(9)	5(2)	13(4)
	D	0.93(9)	2.3(2)	0.6(2)	8(2)	
GE_Cyp	A	0.32(1)	0.35(2)	0.36(2)	76(1)	89(3)

	B	0.39(4)	1.13(7)	0.35(8)	13(2)	
	C	1.0(1)	2.55(8)	0.3(1)	3(2)	11(5)
	D	1.0(1)	1.7(3)	0.5(3)	8(3)	
	A	0.34(3)	0.44(4)	0.49(6)	67(4)	81(8)
GE_Bren_h	B	0.33(7)	1.2(2)	0.4(2)	13(4)	
	C	1.1(1)	2.6(2)	0.7(3)	19(5)	19(5)

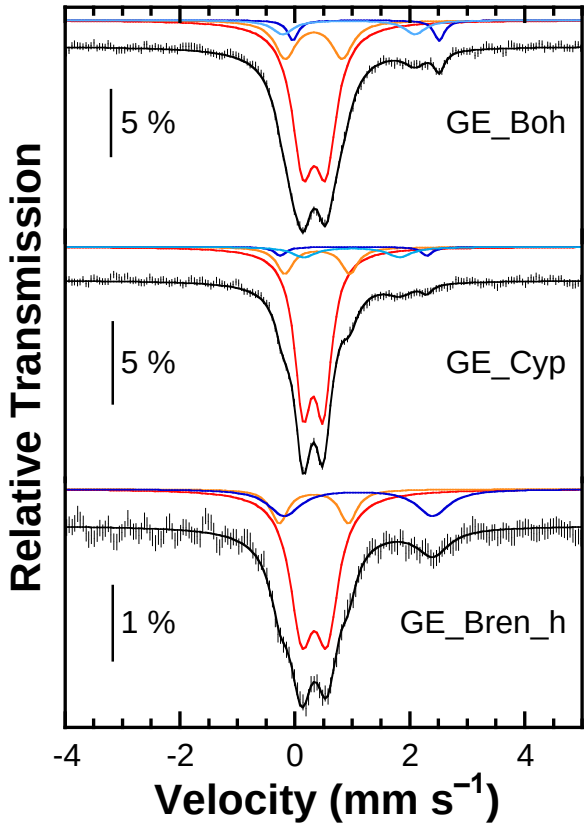

Figure 9: Mössbauer spectra (hatched bars) recorded on GE_Boh (top), GE_Cyp (middle) and GE_Bren_h (bottom) at room temperature. Theoretical spectra are superimposed as solid black lines and the deconvolutions are shown above with sites a in red, sites b in orange, sites c in dark blue and sites d in light blue.

The spectra of Glau_Vil and Cel_Mon are reproduced in Figures S2 and S3, respectively. As expected, that of Glau_Vil is reminiscent of those previously reported for glauconite [46–50], whereas that of Cel_Mon is very similar to those recorded for

celadonite [51–53]. The spectra of GE_Boh and GE_Cyp are reproduced in Figure 9. The comparison with those of Glau_Vil and Cel_Mon (see Figures S2 and S3) suggests that glauconite and celadonite are the main contributors to the Mössbauer spectra of these green earth pigments, respectively. Spectra were reproduced assuming four doublets, labelled a-d. Parameters are listed in Table 7 and Table S1. Doublets c and d are unambiguously associated to ferrous sites according to the isomer shift values. Doublets a and b are assigned to ferric sites. Similar parameters were previously reported in the literature for glauconites [48,54] and celadonites [45,52].

Three doublets were considered to reproduce the Mössbauer spectrum of GE_Bren_h (Figure 9 and Table 7). This historical sample is the sample that presents the highest Fe^{2+} content among the five samples investigated. The nuclear parameters are close to those determined for montmorillonite [45,55]. However, based on the nuclear parameters of site c, other iron phyllosilicates such as illite cannot be excluded. Note that the large line-width may account for several ferrous sites. It should also be noticed that the ferric site b presents the largest quadrupole splitting determined within the investigated series.

3.8 Appraisal of the analysis techniques

The characterization of commercial pigments sold as green earth by different techniques has made it possible to recognize the presence or absence of celadonite or glauconite in certain pigments. The identifications are summarised in Table 8 which show that GE_Cyp and BGE_Cyp contain celadonite, BE_Boh, GE_Rus contain glauconite and that the other pigments contain mainly gypsum and calcite. As some authors [15] have observed, the name of the pigment does not always correspond to the location of the

457 deposit. GE_Bren-h composition, without either of the two minerals, also shows that
458 deposits can evolve over the period in which they were mined as it is observed by
459 Grissom [21].
460

461

Table 8: Summary of the green earth identification by the different techniques

Echantillons	XRD	EDS	mid IR	SWIR	UV-Vis	Mössbauer	Bilan
GE_Boh	Mixed-layer celadonite? Quartz Montmorillonite	Glauconite	Glauconite	Glauconite Montmorillonite	Glauconite ?	Glauconite	**Glauconite** or **Mixed-layer celadonite ?** Montmorillonite Quartz
GE_Cyp	Celadonite Quartz Montmorillonite Calcite	Celadonite	Celadonite	Celadonite Montmorillonite	Glauconite ?	Celadonite	**Celadonite** Montmorillonite Quartz Calcite
BGE_Cyp	Celadonite Montmorillonite Anorthite Anhydrite	Ferroceladonite	Celadonite Gypsum	Celadonite Montmorillonite	Glauconite ?		**Celadonite** Montmorillonite Anorthite Anhydrite
GE_Rus	Glauconite Quartz Calcite	Glauconite	Glauconite	Glauconite Montmorillonite	Glauconite ?		**Glauconite** Montmorillonite Quartz Calcite ?
GE_Ver	Calcite Anorthite	Calcite Montmorillonite	Montmorillonite Calcite	Gypsum Montmorillonite	x		Gypsum Calcite Anorthite
GE_Bren	Gypsum Calcite Montmorillonite Muscovite	Gypsum Calcite Chlorinated compound	Montmorillonite Calcite Gypsum	Calcite Gypsum Montmorillonite	Glauconite ?		**Pigmosol green** Montmorillonite Calcite Gypsum
GE_Nico	Gypsum Calcite Quartz Montmorillonite ?	Gypsum Calcite Cobalt compound	Montmorillonite Calcite Gypsum	Calcite Gypsum Montmorillonite	Celadonite ?		**Hematite** **Cobalt blue** Calcite Gypsum Montmorillonite

GE_Sen	Gypsum Quartz Montmorillonite ? Vanadium borate ?	Calcite Gypsum	Montmorillonite Calcite Gypsum	Calcite Gypsum Montmorillonite	Glauconite ?		**Pigmosol green** Montmorillonite Calcite Quartz
GE_Bren-h	Calcite Quartz Montmorillonite Muscovite Othtoclase	Gypsum Calcite	Gypsum Calcite	Gypsum Calcite	Gypsum	Montmorillonite ?	Montmorillonite Calcite Gypsum

The main aim of these characterisations was to define a methodology in order to be able to identify the minerals in paintings. The accurate in-situ identification of green earth is not easy and the difference between celadonite and glauconite is never considered for paintings (it is more for archeological remains for which cross-sections are more frequently analysed). However such a distinction is now possible, and it is also possible that a specific use of one or the other mineral by an artist can be highlighted in future analyses. Different reasons would explain such a specific use: primarily the origin of the deposit available at the time and in the region would have been taken into consideration. Their various composition, shape, particle-size and hue, would also influence their behaviour with binding media: for instance more or less hydrophilic, different behaviours with water-based media and oils. In summary, for in-situ analysis, as reported previously, several studies have used diverse methods to identify celadonite and glauconite. In the case of modern pigments or that of complex mixtures such identification, and distinction between the two minerals, did not seem relevant:

- If spectrophotocolorimetry and related UV-Visible measurements confirm accurately the presence of green earth, it does not allow one to discriminate glauconite/celadonite. Various earlier studies have used the UV-Visible spectra [17] to identify celadonite and glauconite, this technique was sufficient to discriminate the examples they analysed and it is maybe true for pure pigments but not in more complex cases. However, electronic transitions are seen thanks to absorption bands, i.e. minima in the reflectance spectra. Moreover, in most of the cases, a mixture of phases and addition of organic dyes to enhance the colour are present. The identification of a pigment mixture by their reflectance spectra is sometimes possible but not straightforward as the reflectance spectrum

of a mixture of pigments is not the simple combination of the reflectance spectrum of each pigment.

- NIR is a very convenient method to use for the in-situ identification of green earths. When no signal from other paint components (such as oil) overlaps the characteristic bands, it is possible to distinguish celadonite from glauconite as mentioned in the NIR section.
- Raman microspectroscopy is helpful to focus on specific sample location and hence, being able to evidence additives presence, although Raman has also be used to identify celadonite and glauconite [15].
- The (001) and the (060) reflexions are respectively around 8 and 60° in 2θ, and since they are the main reflections that enable to distinguish celadonite and glauconite, the mobile XRD equipment which is limited in 2θ region going from 12° to 45 °, allows only a difficult and partial identification of the minerals.
- Mobile XRF cannot quantify accurately light cations such as aluminium, magnesium and sodium, especially in the case of complex paint layer stacks. Therefore it is useless for the distinction between celadonite and glauconite.

In the case of sampling, the identification becomes less complex.

- XRD and SEM-EDS can be claimed as the primary techniques that allow a precise identification of both earths due to specific diffraction pattern, shapes, and elemental composition.
- IR spectroscopy is also an appropriate technique to distinguish between celadonite and glauconite due to some specific bands and a better spectrum resolution for celadonite than glauconite.

- Mössbauer spectroscopy can be used to quantify the ratio of Fe^{2+}/Fe^{3+}.

3.9 Application in context

As an application case study, we present here the non-invasive investigation of the composition of green pigments used by Nicolas Poussin in his painting, *Bacchanales d'enfants,* which hangs in the Galleria Nazionale d'Arte Antica (GNAA), Rome.

Figure 10: *Bacchanales d'enfants*, 56 cm x 76 cm, tempera, Nicolas Poussin, 1626, Galleria Nazionale d'Arte Antica (GNAA), Rome, NIR analysed zone in blue: the garland

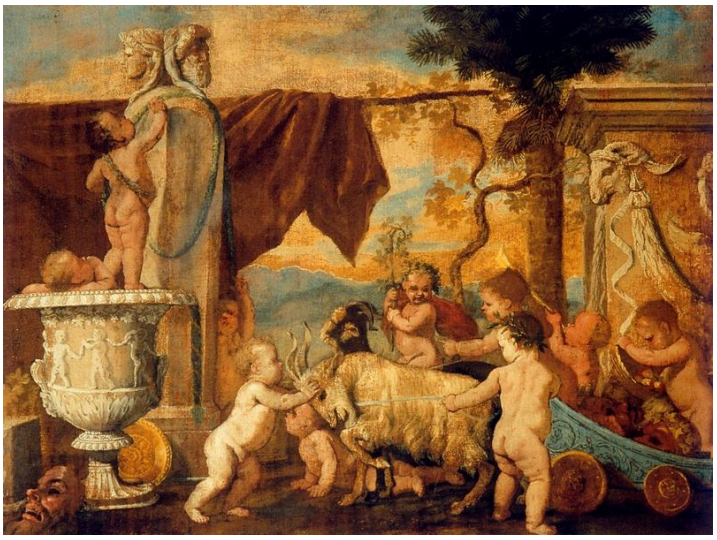

Figure 11 shows the NIR spectra of the green garland (highlighted in Figure 10) compared to reference samples and to two green earths attributed to celadonite and glauconite. The positions of the bands at 2258, 2303 and 2353 nm match better with the positions for the celadonite (2258, 2303 and 2353 nm) than the glauconite (2314 and 2363 nm). Thus, the spectrum of the garland part can be superimposed mainly onto the one of Cel_Mon and GE-Cyp. Even if the application to a painting is quite complex, this part of the *Bacchanales d'enfants* seems to provide a fairly simple NIR spectrum, without gesso, oil or others pigment interaction bands. Therefore, it is possible to identify the pigment used in a tempera painting. In the present case Nicolas Poussin used a green earth originated from a celadonite deposit.

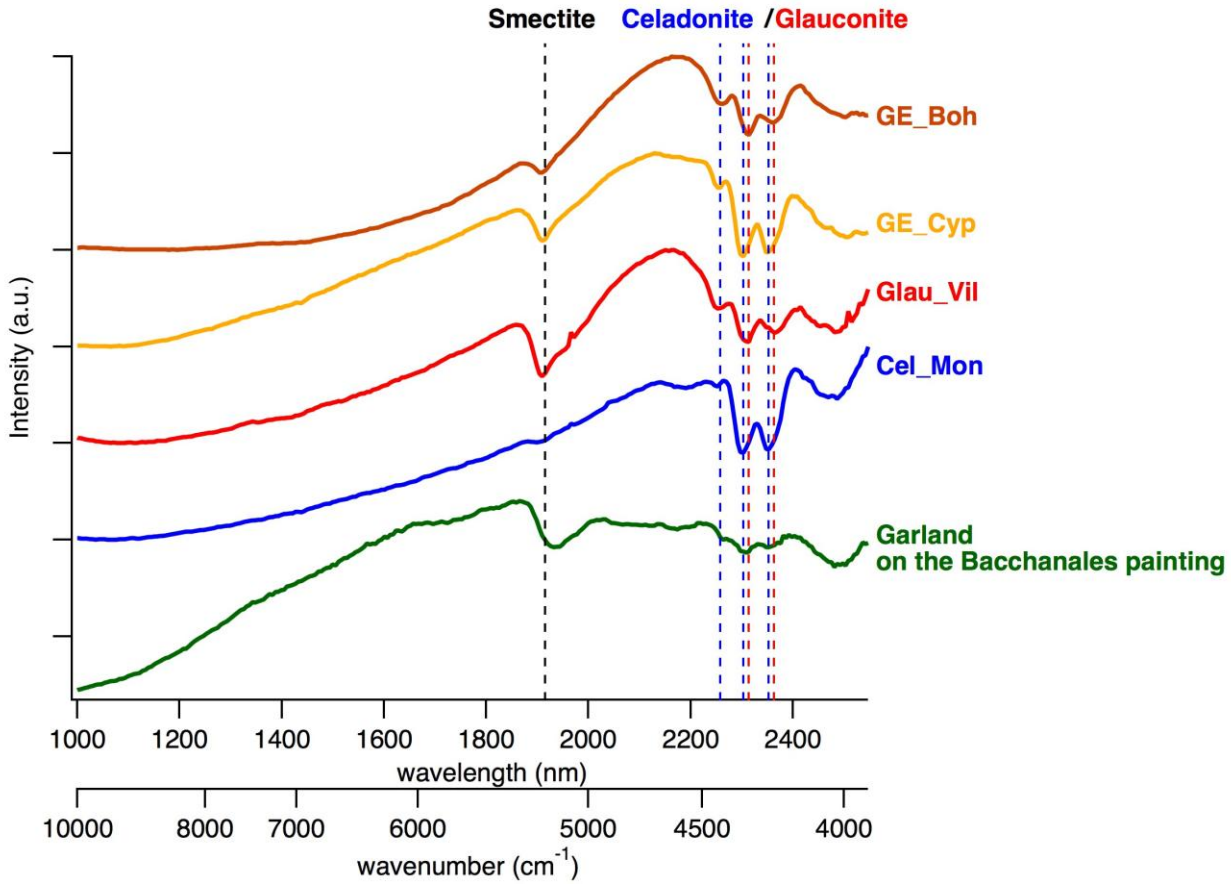
Smectite
Celadonite /Glauconite
GE_Boh
GE_Cyp
Glau_Vil
Cel_Mon
Garland
on the Bacchanales painting
Intensity (a.u.)
1000
1200
1400
1600
1800
2000
2200
2400
wavelength (nm)
10000
8000
7000
6000
5000
4500
4000
wavenumber (cm-1)

528

Figure 11: NIR spectrum of a garland zone in the painting *Bacchanales d'enfants* by Nicolas Poussin (

Figure 10) is compared with reflectance spectra of GE_Cyp and GE_Boh and the reference celadonite (Cel_Mon) and glauconite (Glau_Vil)

4 Conclusion

Eight commercial green pigments sold as green earths were characterized through complementary techniques to assess their composition and crystallographic structure. Some green earths are commercialised as containing mica but after in-depth analysis, they are seen to be composed of gypsum, calcite and organic dyes. XRD and SEM-EDS in the case of sampling, allow precise characterization and identification. Vibrational spectroscopy is the most appropriate method for in-situ characterization. It allows the distinction between celadonite and glauconite. We have shown in the case of Nicolas Poussin's painting, based on NIR analysis, that celadonite was used by the painter for the green garland. This mineral quantification would enable an understanding of paint

properties and the difference between the behaviour of each earth when it is mixed with the binder.

5 Acknowledgment

The authors wish to acknowledge Dr. Cristiano Ferraris of the geological and mineral gallery of the *Museum National d'Histoire Naturelle* (MNHN, Paris, France) for supplying the samples of celadonite and glauconite and the Associate Professor Paolo Bensi of the *Scuola Politecnica Università di Genova* for supplying the more recent sample GE_Bren-h from Monte Baldo, near Prà della Stua.

They are also grateful to Chiara Merucci of the Galleria Nazionale d'Arte Antica (GNAA), Rome, for allowing the analyses of the painting by Nicolas Poussin in the context of their collaboration with the LAMS (CNRS-Sorbonne Université).

The authors thank Catherine Dejoie for the beam time on the beamline ID22 at the European Synchrotron Radiation Facility (ESRF, Grenoble) and her help with the measurements.

This work was supported by the *Observatoire des Patrimoines* of Sorbonne Université (OPUS).

6 Figures

Figure 4: XRD laboratory patterns of two references from mineralogy gallery (Cel_Mon and Glau_Vil), eight commercial green earths and one sample form Brentonico. Most intense diffraction peaks are attributed with: C: Celadonite, G: Glauconite, Gy: Gypsum, Q: Quartz and Ca: Calcite

Figure 5: **a. (top)** Le Bail refinement result for sample GE_Boh (experimental pattern: data points, calculated pattern: red full line, difference: blue full line. The vertical ticks indicate the Bragg positions for celadonite, quartz, montmorillonite, dickite and azurite respectively), Rwp = 18 % (chi2=9.8). The unit-cell parameters obtained for celadonite are: a = 5.2182(11) Å, b = 9.0312(17) Å, c = 10.0180(43) Å, □□= 100**.76**(**4)°**. b. (bottom) Strong hkl-dependent anisotropy of the diffraction profiles of celadonite: see for example broadening of (001) and (110) Bragg reflections.

Figure 6: Rietveld refinement results (experimental pattern: data points, calculated pattern: red full line, difference: blue full line) for samples GE-Cyp (a, top), Rwp = 32 % (Chi2=16.2). The vertical ticks indicate the Bragg positions for celadonite, calcite, quartz and montmorillonite respectively and GE_Bren (b, bottom), Rwp = 25 % (chi2=15.2). Bragg positions for gypsum, calcite, celadonite, quartz and montmorillonite, respectively.

Figure 7: mid-IR reflectance spectra with the main celadonite, calcium, and gypsum attributions in dotted line

Figure 8: NIR spectra of green earths and main band attributions

Figure 9: Mössbauer spectra (hatched bars) recorded on GE_Boh (top), GE_Cyp (middle) and GE_Bren_h (bottom) at room temperature. Theoretical spectra are superimposed as solid black lines and the deconvolutions are shown above with sites a in red, sites b in orange, sites c in dark blue and sites d in light blue.

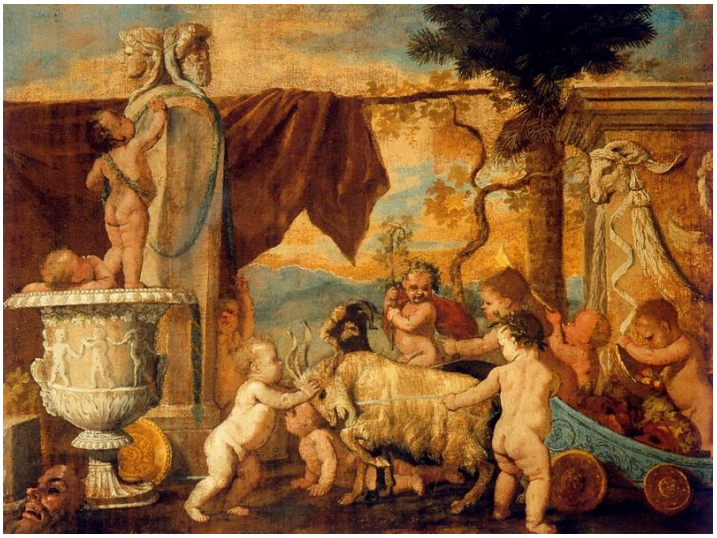

Figure 10: Bacchanales d'enfants, 56 cm x 76 cm, tempera, Nicolas Poussin, 1626, Galleria Nazionale d'Arte Antica (GNAA), Rome, NIR analysed zone in blue: the garland

Figure 11: NIR spectrum of a garland zone in the painting Bacchanales *d'enfants* by

Nicolas Poussin (

Figure 10) is compared with reflectance spectra of GE_Cyp and GE_Boh and the reference celadonite (Cel_Mon) and glauconite (Glau_Vil)

7 Tables

8 References

[1] Douma, M., Pigments through the Ages - Intro to the greens, (n.d.). http://www.webexhibits.org/pigments/intro/greens.html (accessed June 6, 2019).

[2] M. Frizot, L'analyse des pigments de peintures murales antiques. État de la question et bibliographie, ArchéoSciences, revue d'Archéométrie. 6 (1982) 47–59. doi:10.3406/arsci.1982.1192.

[3] Augusti, S., I colori Pompeiani, Roma : De Luca, 1967.

[4] Raehlmann, E., Über die Maltechnik der Alten : mit besonderer Berücksichtigung der römisch-pompejanischen Wandmalerei, nebst einer Anleitung zur mikroskopischen Untersuchung der Kunstwerke, G. Reimer, Berlin, 1910.

[5] F. Delamare, L. Delamare, B. Guineau, G.-S. Odin, Couleur, nature et origine des pigments verts employés en peinture murale gallo-romaine, in: Institut de recherche et d'histoire des textes, Centre de recherche sur les collections, histoire et archéologie Équipe Étude des pigments (Eds.), Pigments et colorants de l'Antiquité et du Moyen Âge : Teinture, peinture, enluminure, études historiques et physico-chimiques, CNRS Éditions, Paris, 2016: pp. 103–116. http://books.openedition.org/editionscnrs/8134 (accessed April 11, 2019).

[6] C. Cennini, G. Tambroni, M.P. (Mary P. Merrifield, A treatise on painting, London, Lumley, 1844. http://archive.org/details/atreatiseonpain00merrgoog (accessed May 19, 2019).

[7] R.E. Van Grieken, K. Janssens, eds., Cultural heritage conservation and environmental impact assessment by non-destructive testing and micro-analysis, Balkema, Leiden, 2005.

[8] D.V. Thompson, C. Cennini, Il libro dell'Arte - English translation The Craftsman's Handbook, Courier Corporation, 1954.

[9] D. Bomford, The National Gallery, eds., Italian painting before 1400: exhibition The National Gallery, London, 29 November 1989 - 28 February 1990, Repr, National Gallery Publ, London, 2002.

[10] K. Groen, PAINTINGS IN THE LABORATORY: Scientific Examination for Art History and Conservation, (n.d.) 24.

640 [11] J.L. Perez-Rodriguez, M. del C.J. de Haro, B. Siguenza, J.M. Martinez-Blanes,
641 Green pigments of Roman mural paintings from Seville Alcazar, Applied Clay Science.
642 116–117 (2015) 211–219. doi:10.1016/j.clay.2015.03.016.
643 [12] H.K.A. Glanville, Some Preliminary Remarks on Nicolas Poussin's Painting
644 Technique in L'Orage: Complementary X-ray Fluorescence and X-ray Diffraction Study,
645 (n.d.).
646 https://www.academia.edu/33508410/Some_Preliminary_Remarks_on_Nicolas_Poussin
647 _s_Painting_Technique_in_L_Orage_Complementary_X-ray_Fluorescence_and_X-
648 ray_Diffraction_Study (accessed June 6, 2019).
649 [13] L. Damjanović, M. Gajić-Kvaščev, J. Đurđević, V. Andrić, M. Marić-Stojanović, T.
650 Lazić, S. Nikolić, The characterization of canvas painting by the Serbian artist Milo
651 Milunović using X-ray fluorescence, micro-Raman and FTIR spectroscopy, Radiation
652 Physics and Chemistry. 115 (2015) 135–142. doi:10.1016/j.radphyschem.2015.06.017.
653 [14] A.M. Cardeira, S. Longelin, S. Costa, A. Candeias, M.L. Carvalho, M. Manso,
654 Analytical characterization of academic nude paintings by José Veloso Salgado,
655 Spectrochimica Acta Part A: Molecular and Biomolecular Spectroscopy. 153 (2016)
656 379–385. doi:10.1016/j.saa.2015.08.043.
657 [15] F. Ospitali, D. Bersani, G. Di Lonardo, P.P. Lottici, 'Green earths': vibrational and
658 elemental characterization of glauconites, celadonites and historical pigments, J. Raman
659 Spectrosc. 39 (2008) 1066–1073. doi:10.1002/jrs.1983.
660 [16] D. Hradil, A. Píšková, J. Hradilová, P. Bezdička, G. Lehrberger, S. Gerzer,
661 Mineralogy of Bohemian Green Earth Pigment and Its Microanalytical Evidence in
662 Historical Paintings, Archaeometry. 53 (2011) 563–586. doi:10.1111/j.1475-
663 4754.2010.00554.x.

664 [17] L.M. Moretto, E.F. Orsega, G.A. Mazzocchin, Spectroscopic methods for the
665 analysis of celadonite and glauconite in Roman green wall paintings, Journal of Cultural
666 Heritage. 12 (2011) 384–391. doi:10.1016/j.culher.2011.04.003.
667 [18] H.A. Buckley, J.C. Bevan, K.M. Brown, L.R. Johnson, V.C. Farmer, Glauconite
668 and celadonite: two separate mineral species, Mineralogical Magazine. 42 (1978) 373–
669 382. doi:10.1180/minmag.1978.042.323.08.
670 [19] S.W. Bailey, Mineralogical Society of America, Micas, Mineralogical Society of
671 America, Washington, D.C., 1987.
672 [20] G.S. Odin, ed., Green marine clays: oolitic ironstone facies, verdine facies,
673 glaucony facies and celadonite-bearing facies ; a comparative study, Elsevier,
674 Amsterdam, 1988.
675 [21] R.L. Feller, National Gallery of Art, eds., Artists' Pigments: a handbook of their
676 history and characteristics. Vol. 1: ..., Repr, National Gallery of Art [u.a], Washington,
677 DC, 2012.
678 [22] P. Piantone, minéralogie et cristallochimiedes phyllosilicates :application à
679 l'étude des altérationshydrothermales, rapport de stage. (1986).
680 http://infoterre.brgm.fr/rapports/86-DAM-019-GMX.pdf (accessed May 6, 2019).
681 [23] D. Hradil, T. Grygar, M. Hrušková, P. Bezdička, K. Lang, O. Schneeweiss, M.
682 Chvátal, Green Earth Pigment from the Kadaň Region, Czech Republic: Use of Rare Fe-
683 rich Smectite, Clays and Clay Minerals. 52 (2004) 767–778.
684 doi:10.1346/CCMN.2004.0520612.
685 [24] D. Hradil, T. Grygar, J. Hradilová, P. Bezdička, Clay and iron oxide pigments in
686 the history of painting, Applied Clay Science. 22 (2003) 223–236. doi:10.1016/S0169-
687 1317(03)00076-0.

688 [25] A.N. Fitch, The High Resolution Powder Diffraction Beam Line at ESRF, Journal
689 of Research of the National Institute of Standards and Technology. 109 (2004) 10.
690 [26] J.-L. Hodeau, P. Bordet, M. Anne, A. Prat, A.N. Fitch, E. Dooryhee, G. Vaughan,
691 A.K. Freund, Nine-crystal multianalyzer stage for high-resolution powder diffraction
692 between 6 keV and 40 keV, in: Crystal and Multilayer Optics, International Society for
693 Optics and Photonics, 1998: pp. 353–361. doi:10.1117/12.332525.
694 [27] J. Rodríguez-Carvajal, Recent advances in magnetic structure determination by
695 neutron powder diffraction, Physica B: Condensed Matter. 192 (1993) 55–69.
696 doi:10.1016/0921-4526(93)90108-I.
697 [28] M. Hellenbrandt, The Inorganic Crystal Structure Database (ICSD)—Present and
698 Future, Crystallography Reviews. (2014). doi:10.1080/08893110410001664882.
699 [29] H. Béarat, Universität Freiburg, eds., Roman wall painting: materials, techniques,
700 analysis and conservation ; proceedings of the International Workshop, Fribourg 7 - 9
701 march 1996, Inst. of Mineralogy and Petrography, Fribourg, 1997.
702 [30] A. Duran, J.L. Perez-Rodriguez, M.C. Jimenez de Haro, M.L. Franquelo, M.D.
703 Robador, Analytical study of Roman and Arabic wall paintings in the Patio De Banderas
704 of Reales Alcazares' Palace using non-destructive XRD/XRF and complementary
705 techniques, Journal of Archaeological Science. 38 (2011) 2366–2377.
706 doi:10.1016/j.jas.2011.04.021.
707 [31] J.F. Bérar, P. Lelann, E.s.d.'s and estimated probable error obtained in Rietveld
708 refinements with local correlations, J Appl Crystallogr. 24 (1991) 1–5.
709 doi:10.1107/S0021889890008391.
710 [32] G. Besson, Refined Relationships between Chemical Composition of
711 Dioctahedral Fine-Grained Mica Minerals and Their Infrared Spectra within the OH

712 Stretching Region. Part I: Identification of the OH Stretching Bands, Clays and Clay
713 Minerals. 45 (1997) 158–169. doi:10.1346/CCMN.1997.0450204.
714 [33] G. Besson, Refined Relationships between Chemical Composition of
715 Dioctahedral Fine-Grained Micaceous Minerals and Their Infrared Spectra within the OH
716 Stretching Region. Part II: The Main Factors Affecting OH Vibrations and Quantitative
717 Analysis, Clays and Clay Minerals. 45 (1997) 170–183.
718 doi:10.1346/CCMN.1997.0450205.
719 [34] I. Garofano, J.L. Perez-Rodriguez, M.D. Robador, A. Duran, An innovative
720 combination of non-invasive UV–Visible-FORS, XRD and XRF techniques to study
721 Roman wall paintings from Seville, Spain, Journal of Cultural Heritage. 22 (2016) 1028–
722 1039. doi:10.1016/j.culher.2016.07.002.
723 [35] J.L. Perez-Rodriguez, M. del C.J. de Haro, B. Siguenza, J.M. Martinez-Blanes,
724 Green pigments of Roman mural paintings from Seville Alcazar, Applied Clay Science.
725 116–117 (2015) 211–219. doi:10.1016/j.clay.2015.03.016.
726 [36] J.L. Bishop, M.D. Lane, M.D. Dyar, A.J. Brown, Reflectance and emission
727 spectroscopy study of four groups of phyllosilicates: smectites, kaolinite-serpentines,
728 chlorites and micas, Clay Minerals. 43 (2008) 35–54.
729 doi:10.1180/claymin.2008.043.1.03.
730 [37] G. Maglione, M. Carn, Spectres infrarouges des minéraux salins et des silicates
731 néoformés dans le bassin tchadien, Cah. ORSTOM. 7 (1975) 3–9.
732 [38] D. Lin-Vien, ed., The Handbook of infrared and raman characteristic frequencies
733 of organic molecules, Nachdr., Academic Press, San Diego, 2006.
734 [39] J.L. Bishop, M.D. Lane, M.D. Dyar, S.J. King, A.J. Brown, G.A. Swayze, Spectral
735 properties of Ca-sulfates: Gypsum, bassanite, and anhydrite, American Mineralogist. 99

(2014) 2105–2115. doi:10.2138/am-2014-4756.

[40] A. Suzuki, S. Vettori, S. Giorgi, E. Carretti, F. Di Benedetto, L. Dei, M. Benvenuti, S. Moretti, E. Pecchioni, P. Costagliola, Laboratory study of the sulfation of carbonate stones through SWIR hyperspectral investigation, Journal of Cultural Heritage. 32 (2018) 30–37. doi:10.1016/j.culher.2018.01.006.

[41] P. Kristova, Spectroscopic techniques for monitoring carbonation reactions and quantification of their products, Brighton, 2016.

[42] S.J. Gaffey, Spectral reflectance of carbonate minerals in the visible and near infrared (0.35–2.55 um): Anhydrous carbonate minerals, J. Geophys. Res. 92 (1987) 1429. doi:10.1029/JB092iB02p01429.

[43] A. Duran, J.L. Perez-Rodriguez, T. Espejo, M.L. Franquelo, J. Castaing, P. Walter, Characterization of illuminated manuscripts by laboratory-made portable XRD and micro-XRD systems, Anal Bioanal Chem. 395 (2009) 1997–2004. doi:10.1007/s00216-009-2992-5.

[44] L. Heller-Kallai, I. Rozenson, The use of mössbauer spectroscopy of iron in clay mineralogy, Phys Chem Minerals. 7 (1981) 223–238. doi:10.1007/BF00311893.

[45] R.E. Vandenberghe, E. De Grave, Application of Mössbauer Spectroscopy in Earth Sciences, in: Y. Yoshida, G. Langouche (Eds.), Mössbauer Spectroscopy: Tutorial Book, Springer Berlin Heidelberg, Berlin, Heidelberg, 2013: pp. 91–185. doi:10.1007/978-3-642-32220-4_3.

[46] C.M. Cardile, Structural site occupation of iron within 2∶1 dioctahedral phyllosilicates studied by57Fe Mössbauer spectroscopy, Hyperfine Interact. 41 (1988) 767–770. doi:10.1007/BF02400503.

[47] E. Kuzmann, S. Nagy, A. Vértes, Critical review of analytical applications of

760 Mössbauer spectroscopy illustrated by mineralogical and geological examples (IUPAC
761 Technical Report), Pure and Applied Chemistry. 75 (2003) 801–858.
762 doi:10.1351/pac200375060801.
763 [48] E. Kuzmann, T.G. Weiszburg, E. Tóth, V.K. Garg, Mössbauer characteristics of
764 glauconitisation, Hyperfine Interact. 186 (2008) 1–8. doi:10.1007/s10751-008-9833-3.
765 [49] M. Skiba, K. Maj-Szeliga, W. Szymański, A. Błachowski, Weathering of glauconite
766 in soils of temperate climate as exemplified by a Luvisol profile from Góra Puławska,
767 Poland, Geoderma. 235–236 (2014) 212–226. doi:10.1016/j.geoderma.2014.07.013.
768 [50] V.A. Drits, L.G. Dainyak, F. Muller, G. Besson, A. Manceau, Isomorphous cation
769 distribution in celadonites, glauconites and Fe-illites determined by infrared, Mössbauer
770 and EXAFS spectroscopies, Clay Minerals. 32 (1997) 153–179.
771 doi:10.1180/claymin.1997.032.2.01.
772 [51] L.G. Daynyak, Interpretation of Mössbauer Spectra of Nontronite, Celadonite, and
773 Glauconite, Clays and Clay Minerals. 35 (1987) 363–372.
774 doi:10.1346/CCMN.1987.0350506.
775 [52] L.H. Bowen, E. DeGrave, D.A. Reid, Mössbauer Study of a California Desert
776 Celadonite and its Pedogenically-related Smectite, 16 (1989) 697–703.
777 [53] L.G. Dainyak, V.A. Drits, L.M. Heifits, Computer Simulation of Cation Distribution
778 in Dioctahedral 2:1 Layer Silicates Using IR-Data: Application to Mössbauer
779 Spectroscopy of a Glauconite Sample, Clays Clay Miner. 40 (1992) 470–479.
780 doi:10.1346/CCMN.1992.0400412.
781 [54] U. Bansal, S. Banerjee, D.K. Ruidas, K. Pande, Origin and geochemical
782 characterization of the glauconites in the Upper Cretaceous Lameta Formation,
783 Narmada Basin, central India, Journal of Palaeogeography. 7 (2018) 99–116.

784 doi:10.1016/j.jop.2017.12.001.
785 [55] J.H. Johnston, C.M. Cardile, Iron Substitution in Montmorillonite, Illite, and
786 Glauconite by 57Fe Mössbauer Spectroscopy, Clays Clay Miner. 35 (1987) 170–176.
787 doi:10.1346/CCMN.1987.0350302.
788 [56] M. Bouchard, A. Gambardella, Raman microscopy study of synthetic cobalt blue
789 spinels used in the field of art, Journal of Raman Spectroscopy. 41 (2010) 1477–1485.
790 doi:10.1002/jrs.2645.
791 [57] D. Cosano, D. Esquivel, C.M. Costa, C. Jiménez-Sanchidrián, J.R. Ruiz,
792 Identification of pigments in the Annunciation sculptural group (Cordoba, Spain) by
793 micro-Raman spectroscopy, Spectrochimica Acta Part A: Molecular and Biomolecular
794 Spectroscopy. 214 (2019) 139–145. doi:10.1016/j.saa.2019.02.019.
795 [58] M.A. Legodi, D. de Waal, The preparation of magnetite, goethite, hematite and
796 maghemite of pigment quality from mill scale iron waste, Dyes and Pigments. 74 (2007)
797 161–168. doi:10.1016/j.dyepig.2006.01.038.
798 [59] T.D. Chaplin, R.J.H. Clark, M. Martinón-Torres, A combined Raman microscopy,
799 XRF and SEM–EDX study of three valuable objects – A large painted leather screen and
800 two illuminated title pages in 17th century books of ordinances of the Worshipful
801 Company of Barbers, London, Journal of Molecular Structure. 976 (2010) 350–359.
802 doi:10.1016/j.molstruc.2010.03.042.
803 [60] C. Charavay, S. Segard, F. Edon, M. Clémancey, G. Blondin (2012) SimuMoss
804 software; CEA/DRF/IRIG, CNRS, Université Grenoble Alpes.

9 For Supporting Information

9.1 Raman

Table S1: Comparative peak positions (in cm^{-1}) of Raman spectra with possible assignments and chemical phases.

Samples main bands Raman shifts									Assignment	Chemical phase
GE_Boh	GE-Cyp	BGE_Cyp	GE_Rus	GE_Ver	GE_Bren	GE_Nico	GE_Senn	GE_Bren-h		
157				150				141		Celadonite[a]
	173	179		189		192		186		Celadonite[a]
						198			δ(Co-O)	Cobalt blue[b]
	215	210								Celadonite[a]
						221			ν(Fe–O sym)	Hematite[c]
					232					
262	272	274	271	258				253		Celadonite[a]
						286			δ (Fe–O sym)	Hematite[c]
					293				ν(Cu-N)	pigmosol
	300	321			335		349	355		Celadonite[a]
				396	390					Celadonite[a]
						399			δ (Fe–O sym)	hematite[c]
						417				
		467				463			δ(O-Si-O) sym (tetrahedron breathing)	Quartz
	489									
						495			ν(Fe–O sym)	Hematite[c]
	499				510		509			
						517			ν(Co-O), ν(Al-O)	Cobalt blue[b]
		560	564	558	547					Celadonite[a]
585	585	589								Celadonite[a]
	610					607			δ (Fe–O sym)	Hematite[c]
						617			ν(Co-O)	Cobalt blue[b]
				637	645					
				672						

					688		688		ρ(CH), δ (C-N-C)	Pigmosol
699	698	701	700							Celadonite [a]
						700			ν(Co-O)	Cobalt blue [b]
					741		741		δ (C-N-C)	Pigmosol [d]
					777		777		ρ(CH),isoindole breath	Pigmosol [d]
					818		818		ρ(CH)	Pigmosol [d]
								893		
	971	960			958		959			Celadonite [a]
					981		981		ρ(CH)	Pigmosol [d]
						989			ν(S-O)	Barite
					1009	1009			V(SO4)	Gypsum
				1086	1086	1086	1086	1087	V(CO3)	Calcite
					1107					
						1137			V(SO4)	Gypsum
								1195		Organic
					1215		1216		δ (CH φ)	Pigmosol [d]
					1283	1283	1286			Pigmosol [d]
					1339		1340		ν(C-N)	Pigmosol [d]
					1447				ν(C-C φ)	Pigmosol [d]
					1506		1506		ν(C-C φ)	?
					1539		1538		ν(C-C φ) ν(CN)	Pigmosol [d]

a: Ospitali [15] ; b: Bouchard [56]; c: Cosano [57], Legodi [58] ; d : Duran [43], Chaplin [59]

9.2 Mössbauer

The Mössbauer spectrum recorded at room temperature on the green earth from Cyprus presents a broad absorption below –1 $mm.s^{-1}$ and above 3 $mm.s^{-1}$ suggesting the presence of a magnetic iron species such as an iron oxide/hydroxide. This contribution was reproduced assuming a parabola, the area accounting for 27±5 % of the total area. This subtraction may further lead to an underestimation of the Fe^{III} content.

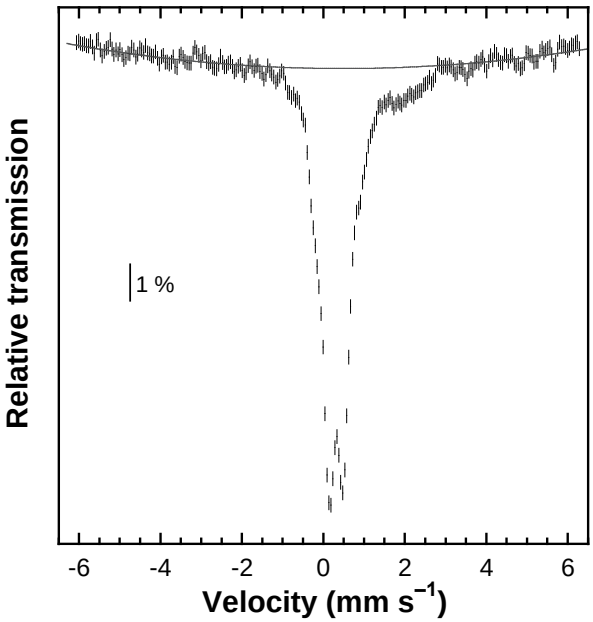

Figure S1: Mössbauer spectrum of GE_Cyp recorded at room temperature (hatched bars). The broad absorption was reproduced by a parabola shown in grey.

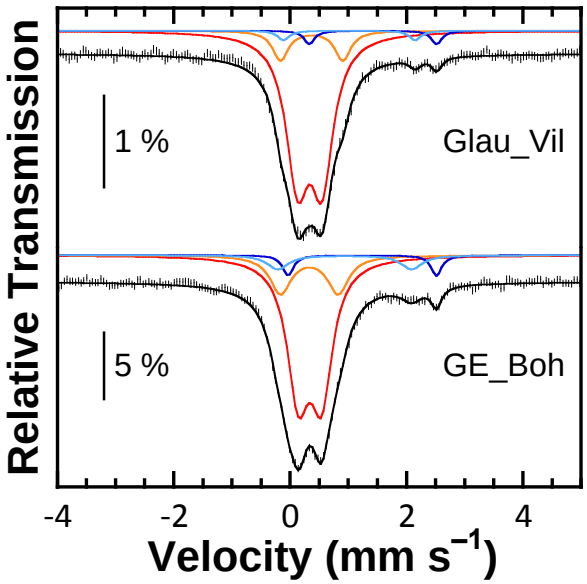

Figure S2: Mössbauer experimental (hatched bars) and theoretical (black solid lines) spectra of Glau_Vil (top) and GE_Boh (bottom). Deconvolutions of theoretical spectra are shown as colored solid lines (sites a-d in red, orange, drack blue and light blue, respectively).

Parameters for Glau_Vil are listed in Table S1 whereas those for GE_Boh are given in Table 8 of the main text.

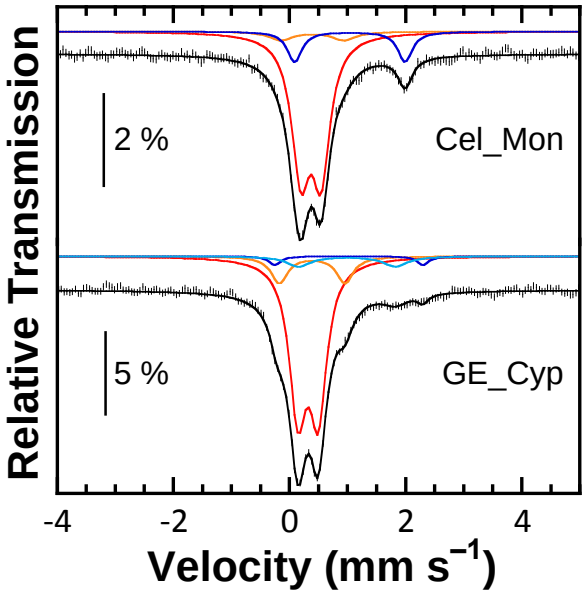

Figure S3: Mössbauer experimental (hatched bars) and theoretical (black solid lines) spectra of Cel_Mon (top) and GE_Cyp (bottom). Deconvolutions of theoretical spectra are shown as colored solid lines (sites a-d in red, orange, drack blue and light blue, respectively).

Parameters for Cel_Mon are listed in Table S1 whereas those for GE_Cyp are given in Table 8 of the main text. Here, only three sites are considered to simulate the spectrum of Cel_Mon. When a fourth site is introduced to reproduce the law absorption detected between 2.5 and 3.0 mm.s^{-1}, its contribution is less than 2%.

Table S2: Parameters used to reproduced spectra of Glau_Vil and Cel_Mon. Uncertainties are indicated in parentheses

Sample	Doublet	δ (mm.s^{-1})	ΔE_Q (mm.s^{-1})	Γ (mm.s^{-1})	%	$\%_{Total}$
Galu_Vil	a	0.34(1)	0.42(2)	0.47(2)	81(1)	93(4)

	b	0.37(5)	1.07(5)	0.32(5)	12(3)	
	c	1.42(6)	2.2(1)	0.22(8)	4(3)	7(6)
	d	1.02(8)	2.3(1)	0.23(8)	3(3)	
	a	0.37(2)	0.35(4)	0.38(5)	79(4)	85(9)
Cel_Mon	b	0.4(1)	1.1(2)	0.5(1)	7(5)	
	c	1.0(1)	1.9(3)	0.3(2)	15(5)	15(5)

838

839